

Advances in laser powder bed fusion of hard-to-weld superalloys: a comprehensive review

Hang You ^a, Guang Fu ^{a,d,*}, Shangkun Jin ^a, Shengliang Luo ^a, Kaifei Zhang ^b, Zhihao Ren ^c, Taiqian Mo ^a, Zhengwen Zhang ^{a,d,*}

^a School of Mechanical Engineering, GuiZhou University, Huaxi district, Guiyang 550025, China

^b Chongqing University of Posts and Telecommunications, China

^c College of Mechanical Engineering, Chongqing University of Technology, China

^d Guizhou Provincial Key Laboratory of Nuclear Components and Materials Manufacturing Technology, Zunyi, Guizhou 563000, China

ARTICLE INFO

Keywords:

Laser powder bed fusion
Hard-to-weld superalloys
Microstructure characteristics
Process optimization
Post-processing
Defect mechanism and control strategy

ABSTRACT

The aerospace industry's demand for superalloys with superior oxidation and hot corrosion resistance has spurred the development of advanced materials for hot-end components. However, traditional manufacturing techniques such as forging and casting, encounter significant challenges due to the complex compositions of these alloys, often leading to processing difficulties and inadequate surface quality. Laser powder bed fusion (LPBF), a digital additive manufacturing technology, presents a viable solution by facilitating the near-net shaping of hard-to-weld superalloys (HWSA). Although LPBF has made considerable progress, its widespread industrial application remains limited. To fully realize the potential of LPBF for producing high-integrity components, this review systematically examines the interplay between microstructural evolution, process parameters, post-treatment techniques, and shaping quality. It also categorizes crack types observed in LPBF-formed alloys and proposes mitigation strategies. Furthermore, the article outlines future research directions to address existing limitations and expand the applicability of LPBF in aerospace manufacturing.

1. Introduction

Nickel-based superalloys, known for their excellent resistance to creep, oxidation, and hot corrosion, are widely used in the manufacturing of aerospace components [1–3]. Traditional casting or forging processing technologies cannot meet the development trend of complex, thin-walled, composite, and integrated parts made from hard-to-weld superalloys (HWSA). Additive manufacturing, as a digital technology that can produce almost any complex geometric shape through layer-by-layer accumulation or particle-by-particle stacking, has been increasingly applied in the aerospace industry [4,5]. Its core methods include Laser Powder Bed Fusion (LPBF), Laser Directed Energy Deposition (L-DED), and Laser Engineered Net Shaping (LENS). LPBF stands out for its advantages in fast, complex, and personalized production. For example, the L-DED technology is suitable for the repair of large-sized components but results in rough surfaces; the LENS technology suffers from issues such as low surface accuracy and material waste; Compared with the LPBF technology, the Selective Laser Sintering (SLS) technology has insufficient mechanical properties of formed

parts and is more suitable for the forming of multi-material or composite materials. Fig. 1 summarizes the advantages of the LPBF technology and the limitations of other additive manufacturing technologies [6–9]. Therefore, the application of the LPBF technology to the preparation of complex nickel-based superalloy components has become the focus of current research and industrialization. This further enhances the value of nickel-based superalloys and significantly propels the development and application of space equipment [10,11], as illustrated in Fig. 2. Moreover, LPBF technology offers higher forming precision and surface quality compared to other metal additive manufacturing technologies, and this technique has been proven to produce near net-shape parts up to 99.9 % relative density [12]. This enables the process to build near-full-density functional parts and has viable economic benefits [13].

A diagrammatic illustration of the principle of operation of the LPBF technique as described by Wu et al. [14] is portrayed in Fig. 3. In the LPBF process, the fabrication begins with the deposition of a thin layer of metal powder onto a substrate plate within a building chamber. Subsequently, a high-energy-density laser is employed to selectively melt and fuse the powder in accordance with the pre-defined digital

* Corresponding authors.

E-mail addresses: gfu@gzu.edu.cn (G. Fu), zwzhang@gzu.edu.cn (Z. Zhang).

model. Upon completion of the laser scanning, the building platform is lowered, and a subsequent layer of powder is deposited, followed by the laser scanning of the new layer. This process is iteratively repeated for successive layers until the desired components are fully fabricated. Consolidation regimes associated with LPBF of high-temperature nickel-based superalloys have been identified for a limited number of alloy systems. The available literature has been systematically evaluated to derive meaningful insights [15,16]. Researchers globally have extensively investigated the LPBF process for superalloys, including IN718 [17–19], IN625 [20,21], and Haynes 230/282 [22–24], elucidating mechanisms such as melt pool dynamics, non-equilibrium solidification, stress-strain behavior, and driving forces. Concurrently, scholars have developed models based on thermal-fluid coupling, thermo-mechanical coupling, and phase field theory to investigate melt pool dynamics, pore defect formation, microstructure evolution, and thermal stress-strain behavior in superalloys such as GH4169 [25] and IN625 during the LPBF process [26,27]. The theories and methodologies associated with the LPBF forming process of these superalloys have reached a relatively advanced stage of maturity. However, with the increase in thrust-to-weight ratio and thermal resistance of the new generation aerospace engines [28,29], traditional superalloys are no longer capable of meeting the performance demands under extreme service conditions exceeding 850 °C [30]. New generations of HWSA, such as CMSX-4 [31] and Rene N5 [32], owing to their unique compositional properties, retain excellent mechanical properties and stability at temperatures exceeding 850 °C, making them a focal point of research in aerospace engine applications [33–35].

Currently, research on HWSA primarily focuses on CM247LC [36,37], IN738LC [38–40], K418 [41], and CMSX-4 [42]. The detailed chemical compositions of these alloys are presented in Table 1. Additionally, Lu et al. [43] investigated the formability characteristics and defects of the difficult-to-weld superalloy GH3536. By comparing numerical simulation results with experimental data, they analyzed the microstructure, mechanical properties, and deformation behavior of GH3536 alloy at room temperature, 750 °C, and 815 °C. Atabay et al. [4] used the LPBF process to fabricate Rene77, achieving a crack-free, dense, and hard-to-weld superalloy via solution treatment and aging, and conducted a comprehensive analysis of the microstructure and tensile deformation behavior at both room temperature and 810 °C. A recurring issue highlighted in these studies is the propensity of materials to crack during the LPBF process. This vulnerability stems from the high mass percentages of elements such as titanium (Ti) and aluminum (Al),



Fig. 2. The advantages of LPBF technology and aerospace applications of HWSA.

based upon the compositions of % Al + 0.84 %Ti (in wt. %) versus 0.28 %Cr + 0.043 %Co (in wt. %), the relationship between the alloy chemistry and the weld susceptibility is illustrated [44]. These elements tend to segregate and accumulate at grain boundaries, resulting in the formation of low-melting-point γ phases [45]. During the LPBF process, which is characterized by significant thermal gradients and substantial thermal stresses, this segregation promotes the formation of pores and cracks [46]. Furthermore, the extreme thermal gradients, ultra-fast solidification rates, and rapid cooling rates inherent to the LPBF process, combined with the effects of remelting, exacerbate crack formation. The LPBF of HWSA presents significant challenges due to their low thermal conductivity and limited fluidity in the molten state. Under high-energy laser irradiation, these materials demonstrate an increased susceptibility to cracking [47]. To address the existing limitations of LPBF-formed HWSA, current research has primarily focused on incremental improvements in traditional process optimization and defect mitigation. Efforts have been made to achieve defect suppression and performance enhancement through microalloying design, process parameter

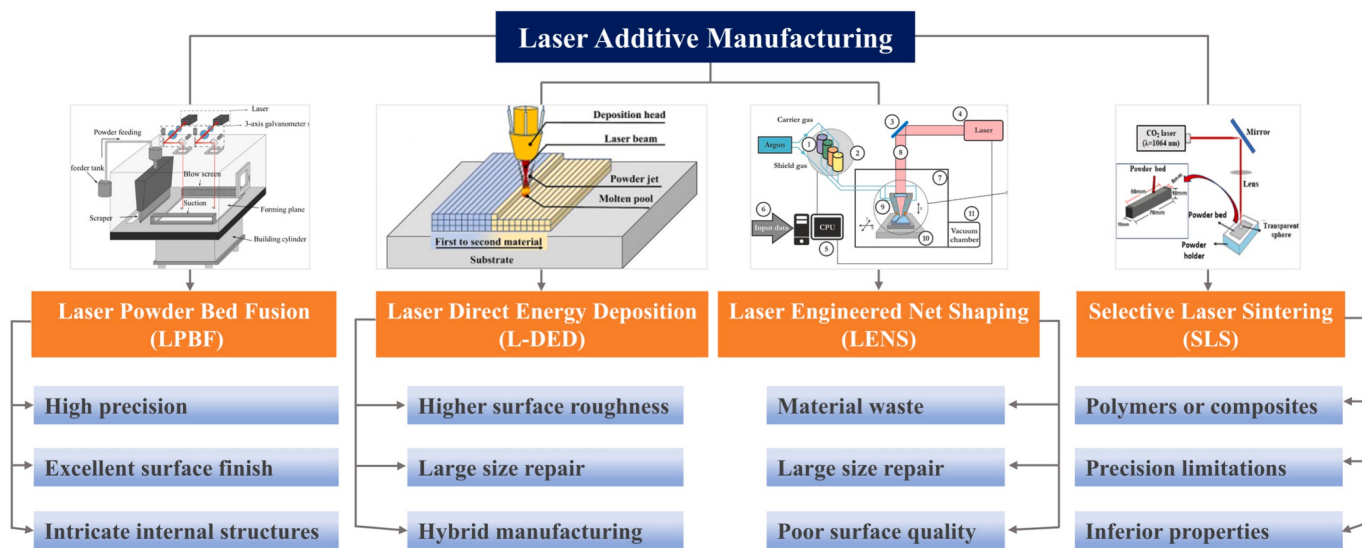


Fig. 1. Typical laser additive manufacturing technologies and their features (reproduced from Ref.[6] copyright 2025 Elsevier Ltd.; reproduced from Ref. [7] copyright 2025 Elsevier Ltd.; reproduced from Ref. [8] copyright 2019 Elsevier Ltd.; reproduced from Ref. [9] copyright 2025 Elsevier Ltd.).

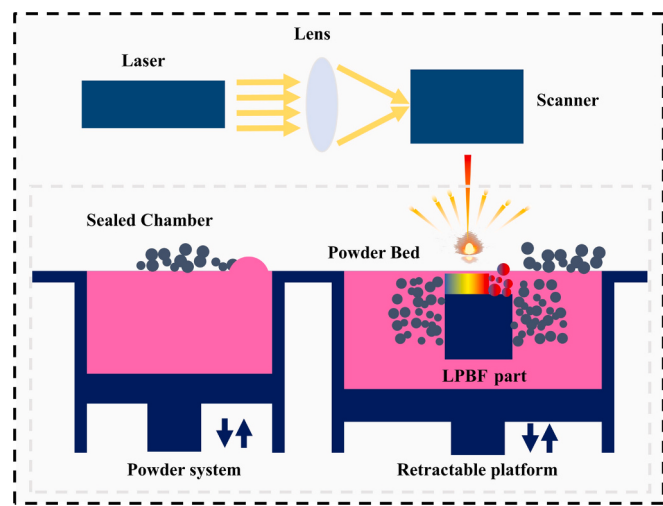


Fig. 3. Schematic of the LPBF process (adapted from Ref. [14] copyright 2021 Elsevier Ltd.).

optimization, and post-treatment methods. In the past two years, researchers have gradually begun to utilize in-situ monitoring [48], multi-physics field coupling simulations [42], composite ceramic particles [49], machine learning [50], and even beam shaping [51] technologies to solve the problems of thermal stress, elemental segregation, and cracking in the LPBF process.

Currently, research on the LPBF process for these materials remains limited and is still in its early stages. Although several review articles have been published on LPBF of metallic materials and high-temperature nickel-based superalloys [52–55], a comprehensive review focusing on the LPBF-based processing of HWSA, a critical material system, remains absent.

Existing reviews have not systematically addressed the unique alloy segregation issues specific to HWSA. The mechanisms underlying the characteristics of the microstructure remain unclear; the optimization of process parameters and post-treatments is overly simplistic; and the scope of performance applications is limited. The objective of this review is to summarize the progress made to date on these alloy systems with a special emphasis on elucidating the relationships between processing, microstructures, defects, post-treatment and forming surface quality, facilitating direct manufacturing of HWSA application in extreme conditions. Therefore, this study systematically reviews the research progress globally on the manufacturing of hard-to-weld high-temperature alloy components using LPBF technology. By integrating findings on high-temperature nickel-based alloys commonly used in LPBF manufacturing, it elaborately introduces the microstructural characteristics and forming parameters of LPBF-formed parts. This paper places particular emphasis on material defects and proposes post-treatment methods to mitigate these defects. Finally, it outlines future research directions for LPBF technology in the field of HWSA.

2. Microstructure characteristics of LPBF-formed HWSA

2.1. Grain morphology

Superalloys frequently encounter a variety of complex service conditions in engineering applications, including sustained mechanical and thermal stresses, corrosive acidic and alkaline environments, and other demanding challenges. The microstructural characteristics of these materials fundamentally influence their macroscopic properties. While research on macroscopic properties has advanced significantly, studies focusing on microstructure and phase composition have increasingly become key areas of interest [56]. Accurate characterization of microstructure and tracking of defect evolution in hard-to-weld nickel-based superalloys are essential for enhancing their high-temperature performance and extending their service life. Furthermore, optimizing post-processing techniques to refine and stabilize the microstructure is equally crucial [57]. Due to the layered fabrication process of LPBF, the cooling rate gradually decreases as the height of the deposited layers increases [58]. At the base of the component, direct contact between the preheated substrates and the powder results in high cooling rates and thermal gradients, which promote the formation of a fine microstructure. As the layer thickness increases, the thermal field within the component undergoes significant changes. The temperature difference between the substrate and the melt pool diminishes, leading to a reduced temperature gradient in the melt pool and resulting in coarser microstructures compared to those in the lower layers. As the temperature gradient keeps decreasing, the coarsest microstructures appear in the topmost layers. Thus, microstructural inhomogeneity emerges along the deposition direction, with upper grain sizes generally coarser than lower ones [59]. This inhomogeneity in microstructure along the build direction, characterized by grain size differences of 2–3 orders of magnitude, directly contributes to mechanical property anisotropy. This anisotropy has become a critical factor limiting the service reliability of complex components. Therefore, it is imperative to achieve microstructure homogenization through dynamic thermal field regulation, such as optimizing laser scanning strategies or employing composite post-processing technologies.

Scanning speed's effect on LPBF was studied. Increasing scanning speed significantly enhances intragranular heterogeneous nucleation, increasing nucleation sites and promoting grain refinement. Mechanical properties initially improve with higher scanning speed but decline beyond the optimal threshold. Optimal performance at 140 W laser power and 1000 mm/s scanning speed yields high relative density and optimal mechanical properties [60]. The heterogeneity of the microstructure is primarily governed by the solidification temperature gradient (G) and the growth rate of the solid-liquid interface (R). The product of G and R , which represents the cooling rate, directly influences the size of the solidified microstructure; higher $G \times R$ values yield finer grain sizes. By adjusting process parameters to control variations in the thermal field and cooling rates, uniform microstructural control can be achieved.

As the deposition height increases, the thermal cycles experienced by the microstructure at varying heights become increasingly complex, resulting in variations in microstructural morphology along the deposition direction [61]. Common microstructures observed include

Table 1
Chemical compositions of LPBF nickel-based superalloys.

Alloy	Chemical compositions													
	Cr	Co	Mo	W	Al	Ti	Ta	Hf	Nb	B	C	Zr	Re	Fe
CMSX-4	7.6	9.3	0.4	2	12.6	1.3	2.2	0.03	—	—	—	—	—	—
IN738LC	16	8.5	1.75	2.6	3.4	3.4	1.7	—	0.9	0.1	0.11	0.05	—	—
CM247LC	8.1	9.2	0.5	9.5	5.6	0.7	3.2	1.4	—	0.015	0.07	0.015	—	—
K418	12.5	—	4.3	—	6.2	0.7	—	—	2.1	0.014	0.12	—	—	1
Rene N5	7.1	8	2	5	6	—	7	—	—	—	—	3	—	—

columnar grains, equiaxed grains, cellular structures, and dendritic formations. The morphological differences among these grains significantly influence the performance of the fabricated components. Due to the preferential growth of columnar grains along specific crystallographic orientations during the solidification process, the material exhibits variations in properties across different direction [62]. Furthermore, the preferred orientation of columnar grains allows certain slip systems to activate more readily along specific directions, thereby contributing to anisotropic behavior. In contrast, equiaxed grains, which have a random orientation, typically exhibit isotropic mechanical properties. This characteristic mitigates anisotropy arising from grain growth direction and enhances property uniformity and structural reliability across orientations. Additionally, the long solute-rich liquid channels between columnar grains promote intergranular thermal cracking. Equiaxed grains, however, generally demonstrate superior resistance to thermal cracking due to their finer grain size and reduced liquid pathway length. Dendrites are a prevalent grain morphology in LPBF-formed materials, particularly in the upper regions of melt pools, where they develop intricate dendritic structures. These dendrites typically form along the boundaries of melt pools due to divergent grain growth directions and impurity segregation at the interfaces, occasionally leading to the formation of equiaxed grains at the margins. Cellular structures are frequently observed in LPBF-formed aluminum alloys, exhibiting a distinctive cell-like pattern that contributes to their unique microstructural characteristics.

Given the layer-by-layer melting and solidification characteristics of the LPBF process, typical microstructural morphologies are illustrated in Fig. 4. Semi-circular rings, which represent the path of the laser beam, are visible on the material surface, followed by the formation of melt pools. The distance between two such rings is defined as the hatch spacing [63]. Various grain morphologies and sizes, including both columnar and equiaxed grains, are observed in Fig. 4(d). Equiaxed fine grains are typically located closer to the fusion line, while columnar grains are situated relatively farther away [64]. This distribution aligns with the unique layer-by-layer solidification mechanism of selective laser melting. However, this typical microstructural distribution is not universal; rather, it is determined by the grain-to-receipt (G/R) ratio [59]. Larger G/R values typically yield finer grain sizes. Early on, Gäumann et al. [65] investigated the microstructural transformation mechanism of the CMSX-4 single-crystal superalloy, as illustrated in

Fig. 5. This conclusion was proposed based on the multi-component alloy solidification theory. Fig. 5a shows that the upper-left region corresponds to the equiaxed grain growth region, while the lower-right region represents the columnar grain growth region. It can be observed that a higher temperature gradient (G) and a lower solidification rate (R) facilitate the growth of columnar grains, whereas a lower temperature gradient and a higher solidification rate promote the formation of equiaxed grains. Thus, achieving an equiaxed microstructure requires minimizing the G/R ratio. This can be achieved by optimizing process parameters, adjusting scanning strategies, and implementing appropriate heat treatment.

The regulation of microstructure size and distribution in IN738 was investigated by adjusting the interlayer rotational speed using three different rotation angles (SS-0, SS-67, SS-90) [66]. Specimens fabricated with 90° and 67° rotations exhibited bimodal grain distributions, while 0° rotation predominantly yielded oriented columnar grains. The grain structure comprised numerous large elongated columnar grains alongside a few small irregular grains (Fig. 6c), as well as many oriented columnar grains (Fig. 6b). The elongated and oriented columnar grains spanned multiple deposition layers parallel to the building direction (BD) and were interspersed with irregular grains located at the boundaries of the columnar grains. Notably, numerous fine equiaxed grain regions surrounded the coarse grain areas. For samples fabricated using 0°, 90°, and 67° scanning strategies sequentially, the aspect ratio of elongated columnar grains decreased, while the proportion of fine equiaxed grains increased, resulting in a more uniform microstructure (Fig. 6f). The results indicate that as the complexity of the heat flow direction increases, columnar grains tend to transform into equiaxed grains, eliminating oriented columnar grains and inhibiting the growth of elongated columnar grains. This underscores the effectiveness of controlling the heat flow direction between consecutive layers through scanning strategies to refine the grain structure of LPBF-formed IN738 alloy [66]. Furthermore, the authors provided a detailed explanation of the grain refinement mechanisms, which include changes in thermal gradients and dynamic recrystallization.

The research team led by Muñoz-Moreno from the University of Cambridge found a significant deviation in grain boundary orientation within the microstructure of the CM247LC alloy formed by LPBF during heat treatment, with a preferred orientation of [001] along the building direction. Heat treatment at temperatures exceeding 1230 °C initiates

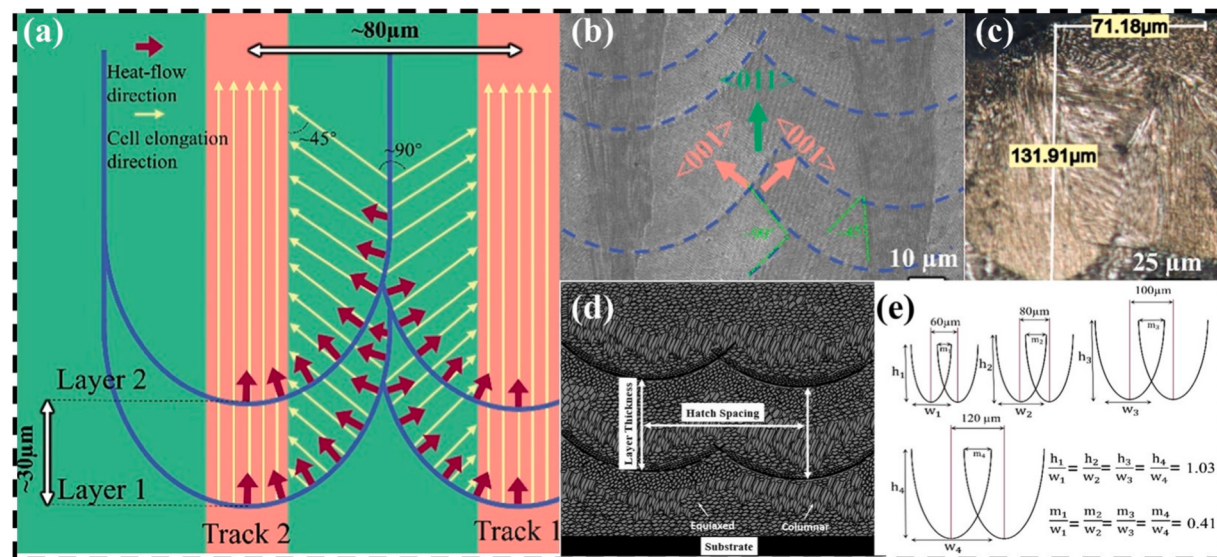


Fig. 4. (a) Schematics of the formation mechanism for the crystallographic lamellar microstructure (CLM); (b) SEM image of CLM corresponds to (a);(c) OM image of CLM showing the melt pool dimension of the top layer. (d)Schematic representation of additively manufactured microstructure of Ni-based superalloys (reproduced from Ref. [63] copyright 2022 Elsevier Ltd.); (e)Results of the derivation of melt pool dimension under different hatch distances (reproduced from Ref. [64] copyright 2025 Elsevier Ltd.).

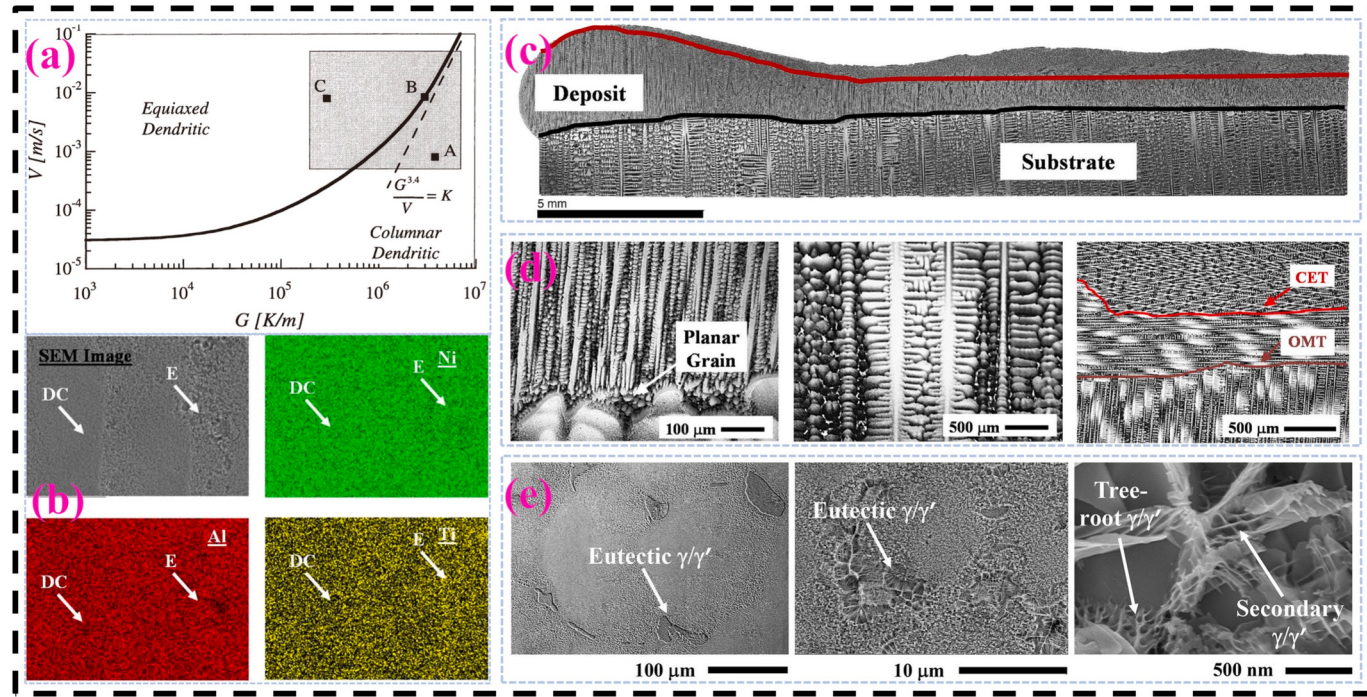


Fig. 5. LPBF process research for CMSX-4: (a) microstructure selection map for superalloy CMSX-4(adapted from Ref. [65] copyright 2001 Elsevier Ltd.); (b) SEM-EDS elemental maps of a representative region in the deposit region; (c) microstructure of printed sections; (d) different grain structure characteristics; (e) precipitation features (adapted from Ref. [31] with permission from the Springer Nature).

recrystallization and promotes the formation of an equiaxed grain structure [67]. The precipitation behavior of the γ' phase and other minor phases varies with increasing heat treatment temperature; similarly, after heat treatment of LPBF-formed K438 [68], numerous similar recrystallized grains were observed in the samples. These recrystallized grains exhibited minimal intragranular distortions and low orientation gradients. Coarse grains were dissolved and subsequently aged, resulting in uniformly sized equiaxed grains. In addition to modulating the microstructural morphology and size of LPBF-formed alloys by adjusting process parameters and post-treatment, some researchers have achieved control through adjustments in elemental composition. For instance, Fig. 7 illustrates the microstructures of IN738LC alloy formed under identical process parameters but with varying carbon content, where typical solidification cellular structures are evident [69,70]. However, the microstructural dimensions differ among alloys with different carbon contents. Overall, as the carbon content increases from 0.11 % to 0.60 %, the grain size decreases to 371.8 nm, indicating the refining effect of carbon on grain structure [71]. This reduction in grain size is likely attributed to the increased precipitation of carbides as the carbon content rises. The impact of these precipitates on the microstructure will be discussed in the following section.

2.2. Precipitated phase

In addition to studying the grain morphology of alloys, the microstructure of HWSA requires particular attention. Understanding the microstructure of these alloys necessitates recognizing their multi-component nature. Nickel-based superalloys typically consist of: (i) a matrix γ phase with a disordered face-centered cubic (FCC) structure, (ii) a precipitated γ' phase with an ordered cubic L1₂ structure, specifically the Ni₃X phase (where X = Al, Ti, Ta), (iii) a γ'' phase with a D022 structure (Ni₃Nb), (iv) carbides, (v) borides, and other phases. Moreover, less desirable topologically close-packed (TCP) phases can also be present in the microstructure, such as: (vi) hexagonal Laves phases [(Ni, Fe, Cr)₂(Nb, Mo, Ti)] and (vii) orthorhombic δ -Ni₃(Nb, Ti) phases [63]. Among these, the γ' and γ'' phases are crucial strengthening components

in HWSA, significantly influencing alloy performance. The γ'' phase is more prevalent in alloys such as IN718, IN625, and Rene220. It is important to note that this phase tends to transform into a stable phase at temperatures above 650 °C, which diminishes the strengthening effect of the secondary phase. Consequently, aging treatments for these materials should be conducted at temperatures below 650 °C to preserve their mechanical properties [72].

When HWSA contain carbon in the range of 0.02–0.2 wt%, carbides can form, enhancing the alloy's strength at elevated temperatures. Carbides located at grain boundaries can inhibit or reduce grain boundary sliding, thereby strengthening the grain boundaries. Additionally, fine carbides within the matrix can further enhance material strength. In nickel-based superalloys, carbides typically exist in three chemical forms: MC, M₂₃C₆, and M₆C [73]. MC carbides are the most prevalent type observed in HWSA at elevated temperatures, appearing as individual particles randomly distributed within the interdendritic regions. Conversely, M₂₃C₆-type carbides predominantly reside at grain boundaries and within grains, positively contributing to the material's high-temperature oxidation resistance and corrosion resistance. To meet the demands of higher operating temperatures, next-generation HWSA must withstand environments of up to 1000 °C. At this temperature, MC carbides can gradually dissolve into M₂₃C₆ and M₆C forms. This reaction can be represented as follows [74]:



High-temperature carbide precipitation, diffusely distributed along grain boundaries, effectively pins dislocations, thereby enhancing grain boundary strength and boosting superalloys' thermomechanical properties. While borides can also strengthen grain boundaries when precipitated, their strengthening effect is constrained by concentration [59]. In LPBF-formed K438 [68], the observed punctiform carbides are predominantly MC carbides. The continuous and semi-continuous elongated carbides located at grain boundaries are rich in chromium and are primarily identified as M₂₃C₆ carbides. After heat treatment,

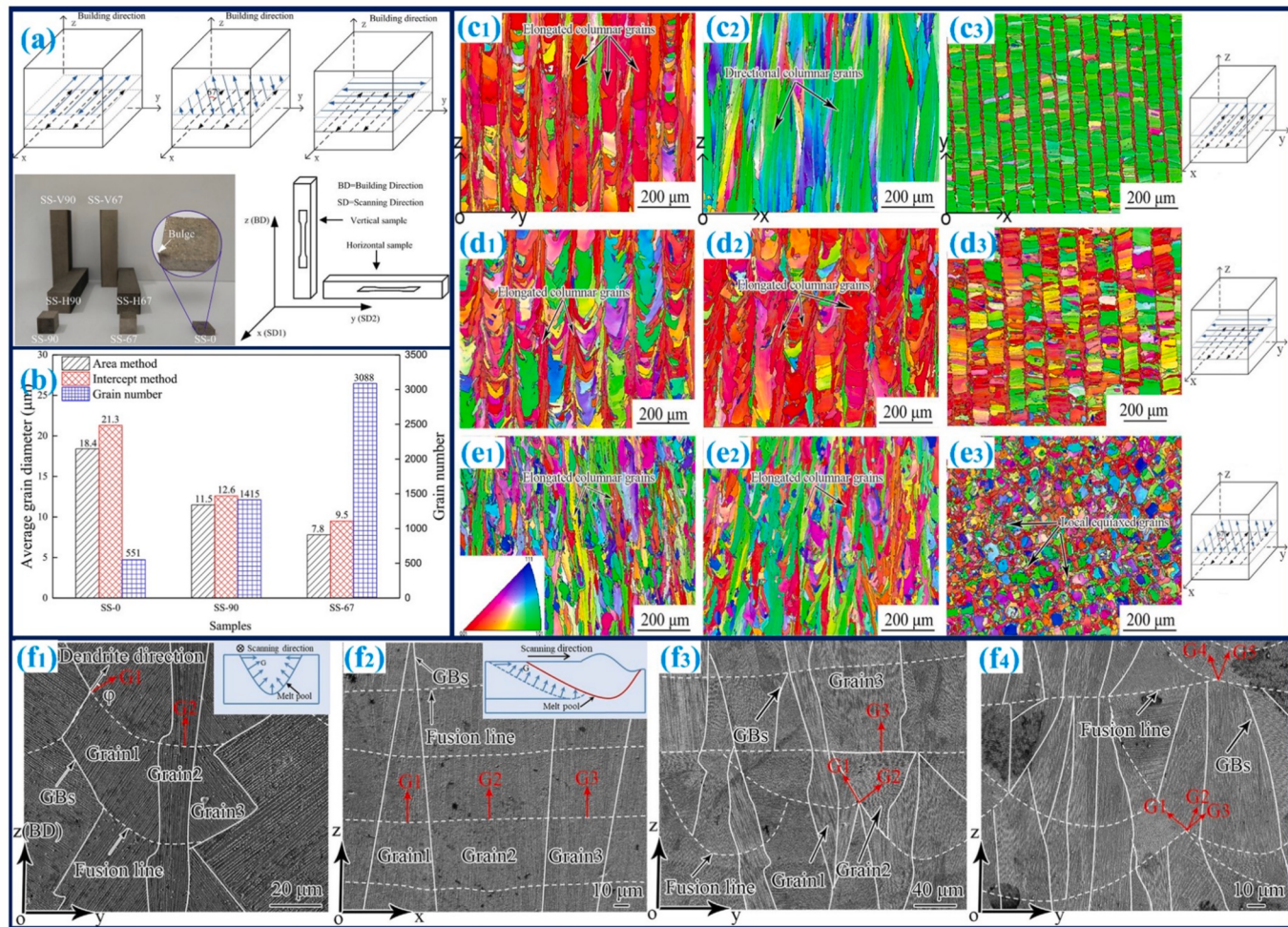


Fig. 6. LPBF-built Inconel 738:(a)Schematics of the scanning strategies and samples; (b)Average grain size in the XZ plane; OIM maps based on IPF of the samples obtained by three scanning strategies in the YZ, XZ and XY planes: (c) SS-0 sample, (d) SS-90 sample, and (e) SS67 sample; SEM of the melt pool morphology and grain structure of the samples, (f1) SS-0 sample in the YZ plane, (f2) SS-0 sample in the XZ plane, (f3) SS-90 sample in the YZ plane and (f4) SS-67 sample in the YZ plane (adapted from Ref. [66] copyright 2021 Elsevier Ltd.).

$M_{23}C_6$ carbides begin to precipitate extensively at temperatures of 1050 °C and 1120 °C, forming a continuous distribution. When the solution treatment temperature exceeds 1200 °C, the $M_{23}C_6$ carbides gradually dissolve from their continuous form and coalesce into MC carbides, effectively enhancing ductility. In HWSA, laves phases (Fe_2Ti/Fe_2Nb compounds) typically form in the weld and heat-affected zones (HAZ), adversely affecting the material's ductility and toughness. Similarly, the η phase (Ni_3Ti), a brittle phase that primarily forms during welding processes, further degrades the material's plasticity and toughness. The presence of the η phase significantly increases the crack sensitivity of superalloys, making them hard to weld. Residual stresses develop during welding due to the considerable hardness of this phase and the disparity in thermal expansion between it and the alloy matrix. Cracks may form when these stresses exceed the material's strength limits. Additionally, the η phase obstructs the movement of dislocations, which diminishes ductility and promotes crack growth. Gases released during the decomposition of the η phase during welding contribute to porosity, thereby weakening the integrity of weld joints. Although the η phase enhances resistance to wear and deformation, it simultaneously reduces toughness and ductility, increasing the likelihood of cracking. Furthermore, the phase's instability in high-temperature and corrosive environments compromises the alloy's ability to resist oxidation and corrosion, presenting significant challenges for its application in demanding conditions.

Variations in volumetric energy density (VED) significantly influence the microstructural characteristics of materials [68]. In the K438 alloy, a high concentration of Al is present in the unique sunflower-like interdendritic regions, where the γ' phase, primarily composed of $Ni_3(Al, Ti)$, is extensively dispersed, thereby enhancing the alloy's mechanical properties. Irregular white particles, ranging from nanometers to micrometers, were observed in these interdendritic regions and identified through EDS analysis as containing high concentrations of Ti, Ta, and Nb. Nb interacts with Al and Ti in the γ' phase, increasing its solvus temperature, while Ta enhances the volume fraction of the γ' phase, thereby improving its strengthening effects. The γ' and γ phases exhibit closely matched lattice parameters, which facilitate coherent strengthening. Additionally, Ti, Ta, and Nb form MC carbides with carbon, which precipitate intra-granularly and at grain boundaries, measuring between 200 and 850 nm. These carbides provide dispersion strengthening; however, when excessively concentrated at grain boundaries, they may lead to thermal cracking, adversely affecting formability. Therefore, balancing carbide distribution is critical for optimizing alloy performance. The γ' phase is essential for the high-temperature performance of HWSA, as it enhances creep resistance and oxidation stability by inhibiting grain boundary sliding and forming protective oxide layers. However, excessive or coarse γ' phases can reduce toughness and ductility, acting as stress concentrators and restricting plastic deformation. Furthermore, the γ' phase increases susceptibility to weld cracking

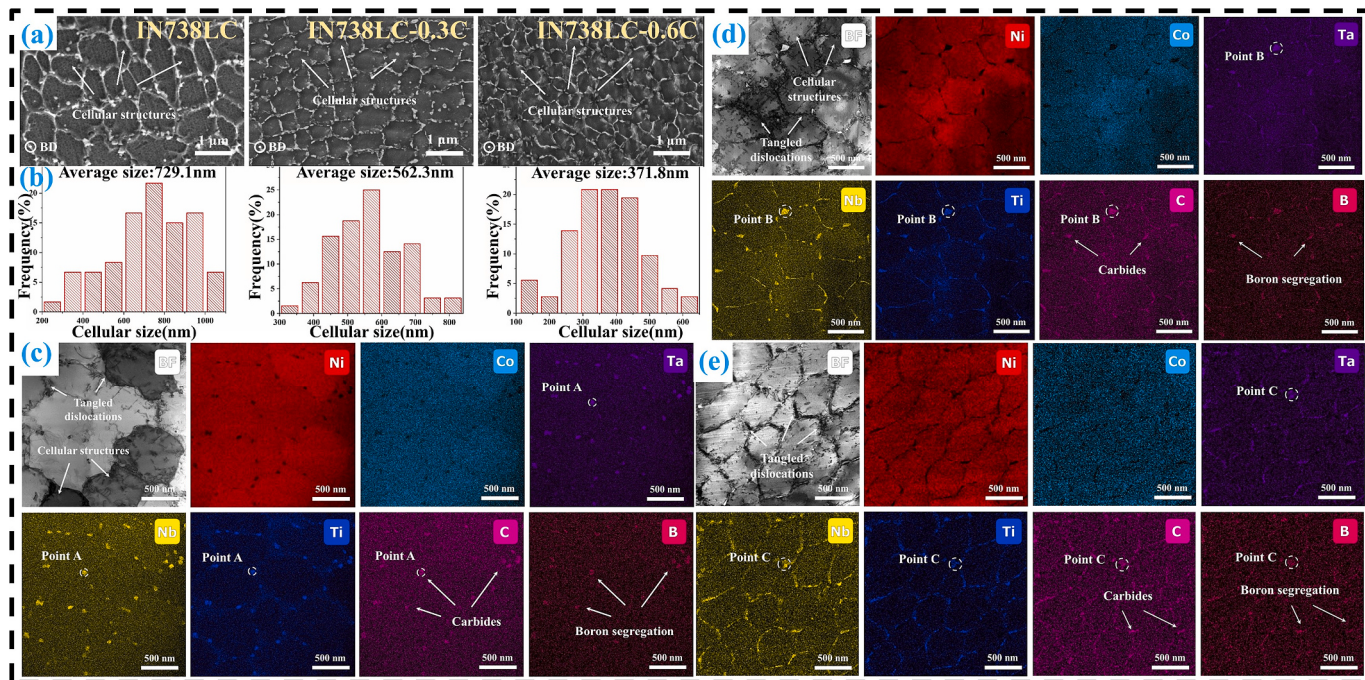


Fig. 7. SEM images(a) and the statistical size distribution (b) of the cellular structure of samples; HAADF, BF and STEM-EDX images of LPBF (c) IN738LC; (d) IN738-0.3C; and (e) IN738-0.6C (adapted from Ref. [71] copyright 2022 Elsevier Ltd.).

due to thermal stress arising from coefficient mismatches and weakened grain boundary cohesion. Thus, optimizing alloy composition, heat treatment, and LPBF techniques is essential for controlling γ' phase characteristics, ultimately improving weld quality and alloy performance in high-temperature applications.

VED is jointly influenced by laser power, scanning speed, layer thickness, and hatch spacing. Cui et al. [75] found that with the increase of VED, the quantity and size of precipitated structures exhibit an upward trend, which is attributed to a relatively slow cooling rate and low degree of undercooling. Furthermore, this study indicated that a finer grain size is associated with maximum microhardness, but the results showed that higher densification degree has the most significant effect on microhardness. Specimens with more defects exhibit the worst microhardness, despite their finer grains. Bandar et al. [76] reported an opposite trend, indicating that higher microhardness was obtained at the lowest VED despite lower relative density. In another study, when VED decreased from 93 J/mm^3 to 46 J/mm^3 , yield stress and tensile strength increased due to the increase of high-angle grain boundaries (HAGBs) and the decrease of cell size, while the work-hardening rate and uniform elongation slightly decreased, and tensile residual stress showed a minor increase [77]. Below 46 J/mm^3 , the mechanical properties of the alloy significantly declined due to the increase in lack of fusion porosity. These results provide evidence for the relationship between VED's influence on grain size and performance. Additionally, VED also affects the texture orientation of precipitated structures: at the lowest energy density value (117 J/mm^3), multi-component textures form due to a high nucleation rate and the presence of defects; at the highest energy density value (1400 J/mm^3), a strong texture in the [100] direction was observed [78], which enhances mechanical properties. Zhao et al. [79] demonstrated through a combination of experiments and finite element analysis that even at the same VED value, different couplings of laser power and scanning speed can generate different thermal histories, leading to grain refinement and higher dislocation density.

This section focuses on the microstructural characteristics of LPBF-formed HWSA, with a focus on the types of grain structures, structural inhomogeneity, the presence of anisotropy, and the influence of precipitated phases on properties. Some researchers have utilized beam

shaping [51] combined with in-situ monitoring [48] to achieve adaptive adjustment of laser energy, thereby mitigating microstructural inhomogeneity, which has great potential in the LPBF process for forming HWSA. In addition, machine learning [50] is applied to the LPBF process for melt pool data collection and feedback to determine the optimal density range. Combining phase-field simulations [42] to explore the precipitation patterns of precipitated phases in HWSA during the LPBF process can avoid the formation of harmful phases.

3. Defects and control strategy of LPBF-formed HWSA

The primary challenge in employing LPBF technology for forming superalloys is the susceptibility of the produced components to defects, including porosity, spheroidization, and cracking. Additionally, the intricate chemical composition of superalloys, comprising elements such as chromium, molybdenum, niobium, and titanium, complicates the welding processes and increases the risk of fractures, ultimately compromising the performance of the parts.

3.1. Formation and suppression of pores

To better elucidate the impact of overall process parameters on metallurgical defects, the concept of laser VED (J/mm^3) has been introduced [80]. VED is defined as the energy delivered by the laser beam per unit volume:

$$E = P/vhs \quad (3)$$

where: P represents the laser power (W); v denotes the laser scanning speed (mm/s); h indicates the layer thickness (mm); and s signifies the scan spacing (mm).

Pore defects are among the most persistent challenges in LPBF processes and the most prevalent type of defect. Two primary types of pores observed in LPBF metal components are lack-of-fusion pores and keyhole pores. Studies have shown that lack-of-fusion pores exhibit irregular shapes, with sizes ranging from micrometers to millimeters. These pores are formed when uneven distribution of powder layers prevents specific regions from receiving sufficient laser energy to

achieve complete melting. Moreover, insufficient energy absorption by the powder, which is influenced by process parameters, can result in insufficient melting, particularly in regions with lower energy density. Poor heat conduction and entrapped gases within the melt pool further contribute to pore formation. As shown in Fig. 8, high laser energy densities (139 and 152 J/mm³) can induce keyhole effects, leading to porosity. Although optimizing process parameters can alleviate pores caused by lack-of-fusion and keyhole phenomena, as supported by prior research, such adjustments alone are insufficient to prevent cracking during the LPBF processing of this alloy. One study showed that adding carbon could yield LPBF samples with less than 0.4 % porosity and no cracks [71]. In a separate investigation of LPBF-formed IN738LC alloy under keyhole conditions, stable keyhole formation correlated with minimal defects. The depth of the keyhole is determined by laser power; higher power increases its depth but may destabilize the process, resulting in pore formation. Under keyhole conditions, heat conduction tends to occur horizontally, causing grains to grow non-perpendicularly to the build direction. Achieving stable keyhole conditions during the LPBF processing of IN738LC [81] necessitates precise control of specific process parameters and selection of appropriate scanning strategies. In their study on the effects of process parameters on porosity, Qiu et al. [82] showed that defects are highly sensitive to laser scanning speed. At higher scanning speeds, pores increase in size and number, take on elongated shapes, and are predominantly located at interlayer boundaries. Calandri et al. [83] observed an unusual concentration of pores near sample edges associated with the highest VED values, occurring at scanning speeds exceeding 600 mm/s. At lower VED levels, porosity was most pronounced, as shown in Fig. 8(a), characterized by numerous large, irregular voids primarily resulting from lack-of-fusion. To mitigate this issue, an appropriate increase in laser power while maintaining the same scanning speed and hatch distance can help reduce occurrences of lack-of-fusion. Notably, samples produced with intermediate VED values exhibited no significant porosity anomalies.

Laser energy density plays a crucial role in defect formation during LPBF of HWSA. Pores typically exhibit spherical or ellipsoidal shapes. Deviations from the optimal laser energy density can result in insufficient melting, excessive vaporization, or unstable melt pool heights. Excess energy input may trigger strong convection and vapor recoil, leading to jet splashing and process instability. For the K438 alloy after heat treatment, it has been found that as the VED increases, the porosity density rises while the pore diameter decreases [68]. This phenomenon occurs because a higher VED accelerates the volatilization or removal of gases and moisture in the powder, thereby increasing the density of the

sample. Additionally, smaller pores can help mitigate cracking in the sample. However, high laser energy density during scanning may induce keyhole formation, characterized by irregular cavities that can significantly degrade the mechanical properties of the material, leading to the evaporation of low-melting-point elements. When subsequent powder layers cover these areas, irregular keyholes may form. Reducing the input energy can help control this phenomenon.

Although optimizing VED can maintain extremely low porosity, in high Al and Ti content HWSA, the increased melt viscosity and reduced thermal conductivity complicate porosity suppression. Studies have shown that multi-physics field coupling modeling [42] combined with in-situ monitoring [48] technology can dynamically predict and adaptively control pore formation, representing a mechanistic approach to pore suppression. This technology demonstrates significant application prospects in the LPBF processing of HWSA.

3.2. Mechanism of crack formation and control strategies

HWSA are widely favored for aerospace engine blades and gas turbines due to their exceptional thermal stability and resistance to hot corrosion [84]. Nickel-based superalloys maintain superior mechanical and physical properties at temperatures ranging from 540 °C to 1000 °C. Despite their excellent high-temperature performance, these alloys are prone to significant cracking during the rapid solidification and contraction phases of LPBF processing, primarily due to precipitation and thermal stresses. The high content of Al and Ti (Al + Ti > 6 %) in these alloys, where γ' serves as the strengthening phase, increases brittleness during formation, thereby adversely affecting the final material properties [85]. Cracking in these HWSA can be categorized into four main types: solidification cracking (SC), liquation cracking (LC), ductile-dimple cracking (DDC), and strain-age cracking (SAC) [86–88]. In LPBF HWSA, particular attention is given to the first two types of cracks [86,89], as illustrated in Fig. 9.

Liquefaction cracking is a common issue in superalloys, primarily linked to the segregation of alloying elements. In the case of the K438 alloy [90], rapid cooling causes elements like Al and Ti, which contribute to the formation of the γ' phase, to accumulate in the interdendritic liquid phase. These elements precipitate as γ' and $\gamma-\gamma'$ eutectic mixtures at grain boundaries, leading to localized compositional variations. This segregation results in an uneven distribution of solute elements within the solidification zone, where the non-uniform γ' phase can diffuse into the matrix and re-dissolve during subsequent melting. The high cooling rate restricts this diffusion. Consequently, regions that

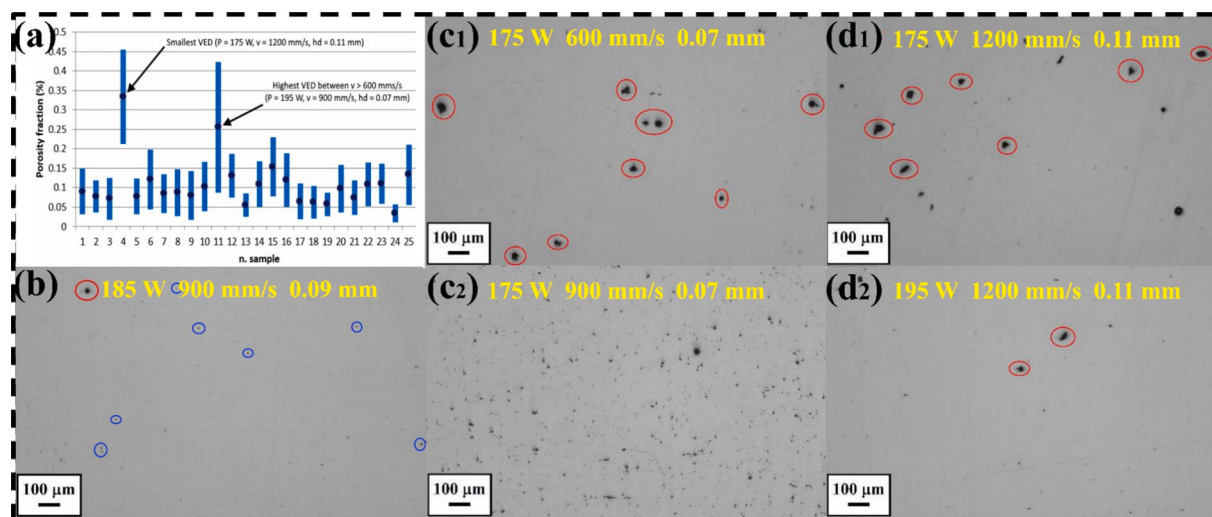


Fig. 8. (a) Porosity fraction of different samples;(b) Optimal process parameters;(c) Comparison of scanning speeds;(d) Comparison of laser powers (adapted from Ref. [83] under a Creative Commons Attribution-Noncommercial License).

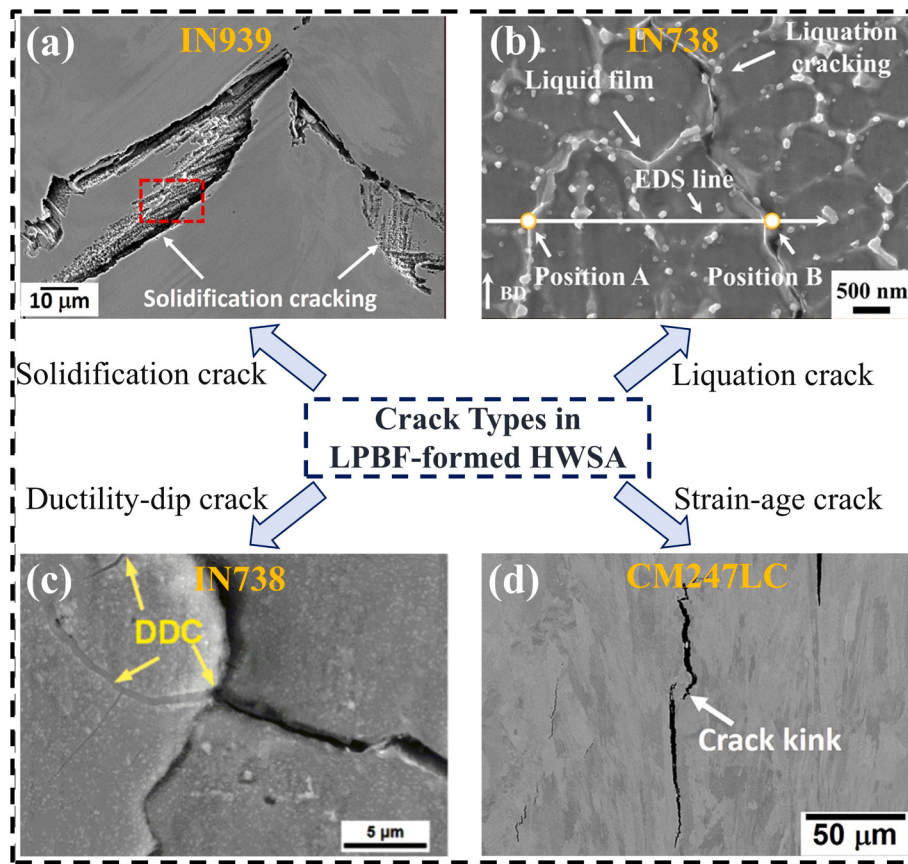


Fig. 9. Main crack types in LPBF-formed hard-to-weld superalloys: (a) Solidification cracks (reproduced from Ref. [89] copyright 2021 Elsevier Ltd.); (b) liquation cracks (reproduced from Ref. [71] copyright 2022 Elsevier Ltd.); (c) strain-age cracks (reproduced from Ref. [89] copyright 2021 Elsevier Ltd.); (d) ductility-dip cracks (reproduced from Ref. [86] copyright 2021 Elsevier Ltd.).

typically contain MC or γ phases become surrounded by areas with higher concentrations of MC or γ phases, forming thin films of low-melting-point eutectic constituents along the grain boundaries. The presence of these films facilitates liquation at the grain boundaries during melting. However, these liquated boundaries lack the strength to

withstand applied stresses, ultimately resulting in liquation cracking [85,90]. Zhao et al. [91] made similar observations, noting that LPBF-formed Rene88DT samples exhibit significant liquation in crack areas, characterized by a brittle intergranular fracture pattern. EDS analysis revealed that the re-solidified material within these cracks contains high

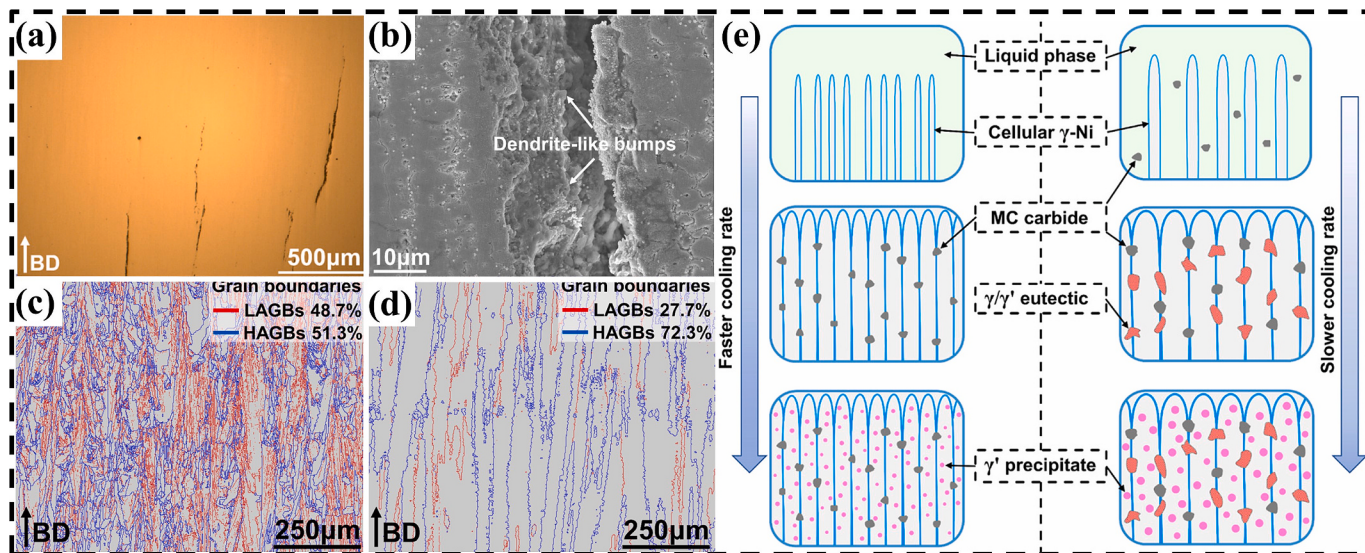


Fig. 10. Typical distribution characteristics of LPBF-formed ZGH451: (a) the OM images of the specimen; (b) crack morphology; grain boundary distributions under (c) low laser power and (d) high laser power; (e) the microstructure evolution processes of the different laser power (adapted from Ref. [93] copyright 2021 Elsevier Ltd.).

concentrations of Ti, Al, Cr, Co, and Ni, indicating the development of eutectic phases. During the final stages of solidification, low-melting-point phases are prone to forming at grain boundaries [92] or within dendritic structures. A defining feature of liquation cracks is the presence of a liquid film. During the high-energy beam additive manufacturing (HEB-AM) process, such films commonly develop in the interdendritic zones of the HAZ or along grain boundaries.

The microstructural and defect characteristics of ZGH451 fabricated via LPBF [93] are shown in Fig. 10. Cracks initiate from the molten pool base, propagate along the building direction, and typically span multiple layers. These cracks were identified as solidification cracks (Fig. 10a) and exhibit intergranular characteristics. The research team found that the misorientation angle between adjacent grains exceeds 15° , indicating a preference for HAGBs. These cracks form in the semi-solid region during the final stages of solidification, where shrinkage stresses disrupt the interdendritic liquid film [94,95]. Stress concentrations at grain boundaries, driven by disparities in crystallographic orientation, further promote crack initiation. Consequently, crack formation in ZGH451 is closely linked to thermal stress conditions and the solidification microstructure. Optimizing process parameters is critical for mitigating these defects and enhancing the integrity of the components.

The impact of process parameters on crack formation has been thoroughly examined. At a laser power of 200 W, a VED greater than 166 J/mm^3 resulted in cracks exceeding $200 \mu\text{m}$ in length. However, reducing the VED to a range of $83\text{--}139 \text{ J/mm}^3$ shortened the cracks to approximately $100 \mu\text{m}$, aligning them with the build direction. While insufficient energy density led to unfused defects, it also minimized cracking [95]. Crack-free samples were achieved at the optimal VED, as lower energy densities reduce thermal stress [96,97] and accelerate cooling, which refines the microstructure [98,99] and enhances stress resistance. A high VED increases susceptibility to cracks, which

correlates with larger grain sizes, whereas finer microstructures are better able to accommodate solidification stresses [100,101]. Additionally, silicon segregation at grain boundaries further promotes cracking [102]. Therefore, optimizing energy input and cooling rates is essential for achieving defect-free LPBF fabrication of the ZGH451 alloy. In contrast, LPBF studies of the K438 alloy demonstrated that a lower VED ($64\text{--}74 \text{ J/mm}^3$) at 270 W power resulted in cracks measuring $200\text{--}700 \mu\text{m}$, oriented parallel to the build direction. Increasing the VED to 86 J/mm^3 reduced both the frequency and dimensions of the cracks, as higher energy densities promote more uniform heat distribution, reduce thermal gradients, and alleviate stresses. Furthermore, employing alternating scan strategies and rotating layers by 67° enabled nearly crack-free fabrication [66]. These findings indicate that optimal process parameters are material-specific, highlighting the necessity of developing LPBF crack-free databases for refractory superalloys. Tailoring energy input and utilizing advanced scanning techniques are crucial for optimizing defect-free fabrication across diverse materials.

Alloy composition control is a crucial strategy for mitigating cracking in LPBF. By reducing Ti content and incorporating elements such as Ta and Hf, the AM80 alloy [103] has been successfully engineered to exhibit excellent formability with diminished cracking tendencies. In the case of CM247LC, the removal of Hf narrows the solidification range, increases the presence of interdendritic MC carbides, and reduces thermal sensitivity. Additionally, lowering Al content decreases the fraction and size of the γ/γ' eutectic phase, alleviating stress concentrations and enhancing crack resistance [104]. Furthermore, reducing Zr and B concentrations effectively minimizes crack formation [105]. SEM images (Fig. 11a) reveal solidification cracks at dendrite arms due to insufficient liquid filling and residual stresses [106] in IN738LC alloys, as well as liquation cracks at grain boundaries, which are often associated with boron segregation [71]. The

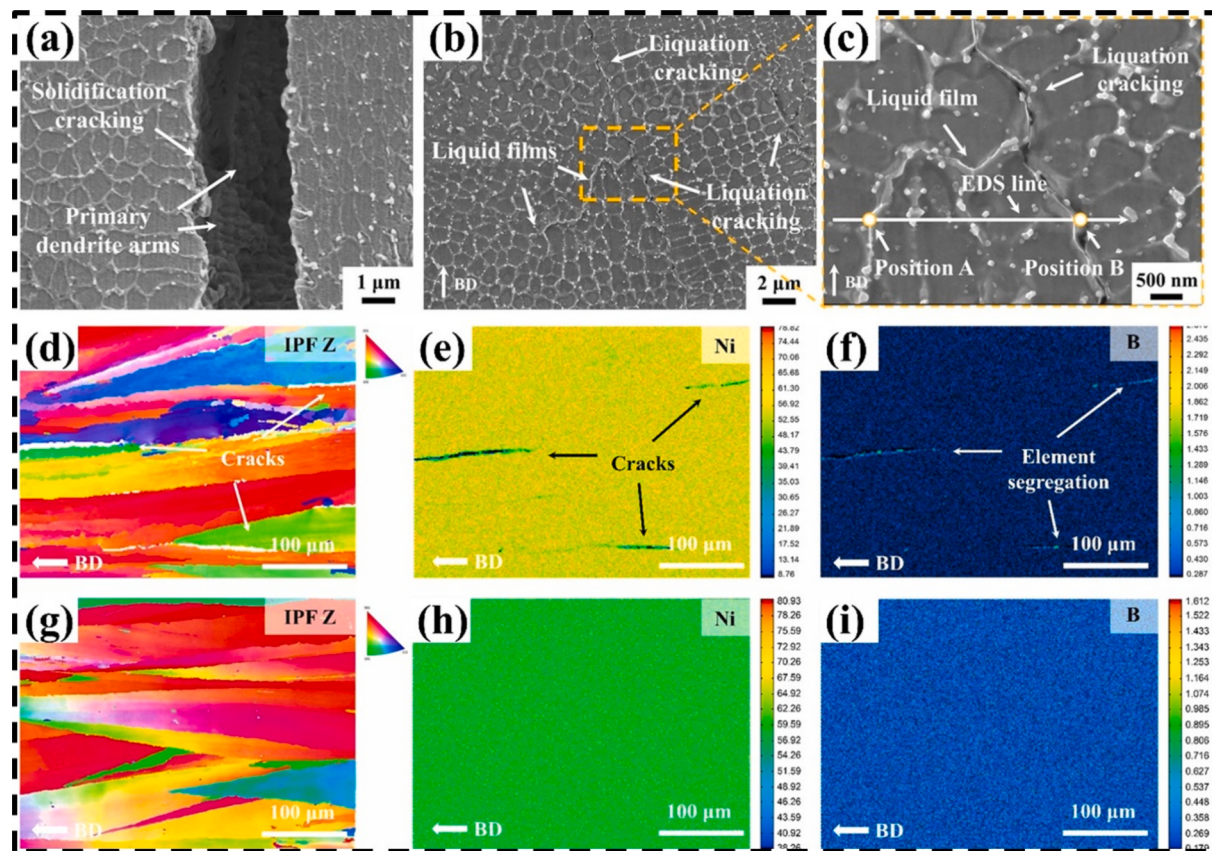


Fig. 11. (a)The SEM image of fracture surfaces of open cracks of the LPBF IN738LC exhibiting the dendritic morphology;(b, c) The SEM images of liquation cracking in IN738LC via LPBF with liquid films; (d-f) IPF and EPMA maps of IN738LC and (g-i) IN738-0.3C via LPBF (reproduced from Ref. [71] copyright 2022 Elsevier Ltd.).

addition of carbon to modify the matrix suppresses hot cracks, while smaller eutectic and low-melting phases reduce both solidification and liquation cracks. These compositional adjustments underscore the significance of tailored alloy design for achieving crack-free LPBF fabrication. Beyond investigating the effects of trace elements and process parameters on cracking, Grange et al. [107] employed various microanalysis techniques to observe cracks, melt pools, and microstructures, facilitating quantitative crack analysis. Although solidification cracks and liquation cracks are not entirely distinct phenomena, they can interact with one another. Xu et al. [108] examined their interplay in LPBF-formed IN738 samples, noting that grain boundary carbides induce stress concentrations and impede liquid flow, thereby promoting the formation of liquation cracks near these carbides. During subsequent layer deposition, columnar grains grow epitaxially, and crack tips from previous layers persist as stress concentrators. Insufficient liquid metal prior to solidification allows solidification cracks to merge with liquation cracks, propagating “epitaxially” into new layers [41]. This interplay highlights the necessity of controlling solidification dynamics and minimizing grain boundary carbides to prevent crack formation and propagation in LPBF processes.

To summarize, liquation cracks are prevalent in poorly weldable nickel-based superalloys such as IN738, K465, and CM247LC. These cracks are characterized by intergranular cracking, significant elemental segregation, and the formation of liquid films [109,110]. Their development necessitates both the presence of a liquid film and residual tensile stress that exceeds a critical threshold (Fig. 12a). Mitigation

strategies include reducing grain boundary segregation, minimizing the presence of low-melting-point phases, decreasing the number of HAGBs, and alleviating residual stress [109–111]. Solidification cracks, which are characterized by wide gaps and cellular or dendritic patterns, occur in the mushy zone as a result of high thermal gradients and rapid cooling. Insufficient liquid feeding, often attributed to the presence of carbides and large dendrites, contributes to the formation of these cracks (Fig. 12b). By redesigning alloys to enhance solid solution strengthening and incorporating trace elements, it is possible to narrow the solidification range, reduce cracking sensitivity, and improve high-temperature performance [106,112].

This part elaborates on the main defects and control strategies of LPBF-formed HWSA. In the study of pores, porosity can be reduced by optimizing process parameters or adjusting compositions. For crack control, it can be achieved by regulating VED, optimizing scanning strategies, adjusting compositions, and other methods. Constructing a multi-physics field coupling model [42], combined with in-situ monitoring technology [48], to develop a dynamic pore prediction and laser energy adaptive adjustment system can achieve precise pore suppression. Integrating machine learning [50] to realize crack early warning and real-time process optimization is another research direction. In addition, preliminary studies have explored the application of micro-alloying methods with ceramic reinforcing phases [49] added in the LPBF forming of nickel-based alloys, which can prevent crack propagation by inhibiting interface reactions. This method can provide certain ideas for the LPBF process of HWSA.

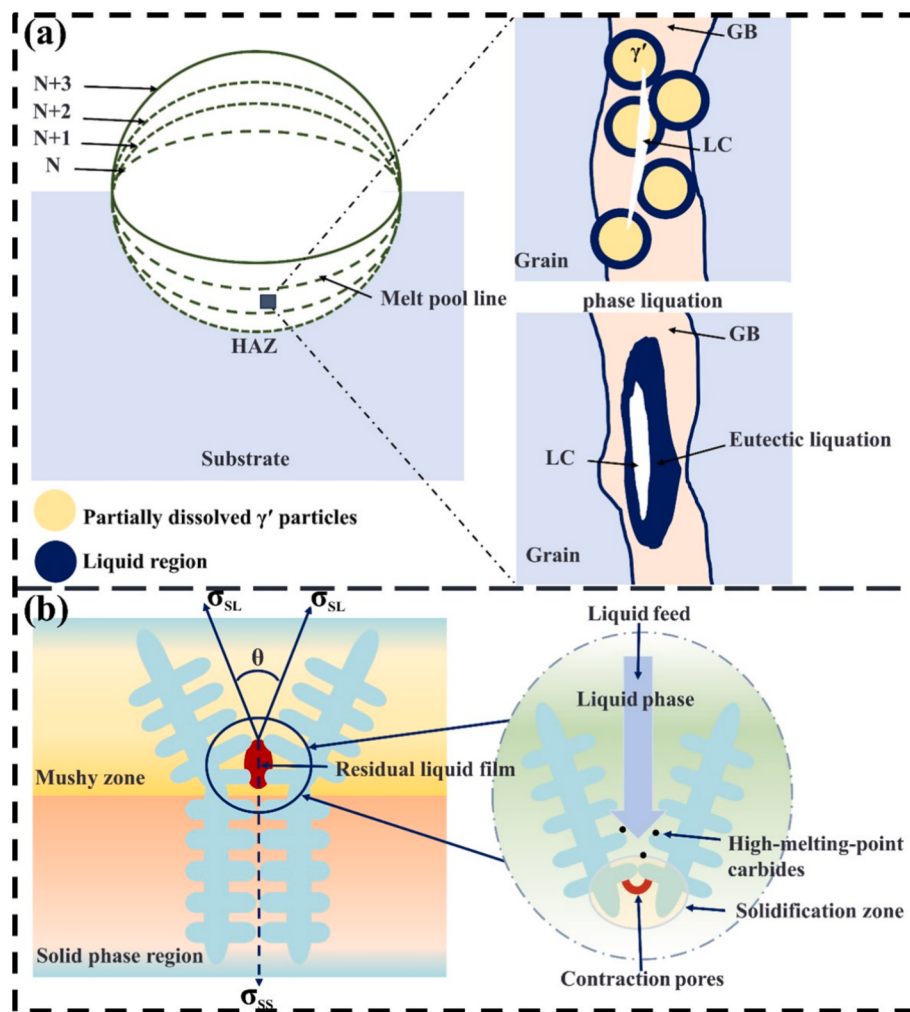


Fig. 12. Schematic diagram of cracks formation mechanism: (a) liquation cracks (adapted from Ref. [109] with permission from the Springer Nature); (b) solidification cracks (adapted from Ref. [110] under a Creative Commons Attribution-Noncommercial License).

4. Process parameters of LPBF-formed HWSA

Superalloys are extensively utilized in hot-end components due to their exceptional properties. However, they contain a high proportion of γ' -phase-strengthening elements (Al, Ti) and refractory metals (W, Mo), which make them susceptible to issues such as hot cracking, liquefaction cracking, and elemental segregation during welding. By leveraging the rapid solidification characteristics of layer-by-layer melting, LPBF can effectively suppress macroscopic elemental segregation, form a supercellular substructure, and significantly enhance the room-temperature mechanical properties of the alloy. Key process variables, such as laser power [113–115], scanning velocity [64], layer thickness [116], and scanning strategy [117,118] play a critical role in LPBF-formed HWSA. However, different superalloy compositions exhibit significantly varied responses to these process parameters, and a universal optimization model is still lacking. Furthermore, the mechanisms through which the coupling of multiple parameters (power, velocity, and scanning strategy) influences dendrite orientation and phase distribution remain poorly understood. Based on these challenges, this study investigates the relationship between specific LPBF parameters and the properties of typical refractory superalloys. Achieving optimal process conditions is essential for manufacturing defect-free, high-performance components from HWSA. By precisely adjusting these variables, the solidification pathway can be controlled, thereby minimizing segregation and defects while enhancing material consistency and reliability. Grange et al. [107] examined the impact of melt pool geometry on defect formation in LPBF-formed IN738LC and identified that narrow melt pools with high overlap are optimal for minimizing cracks. Key metrics, including melt pool width (W_{MP}) and remelted zone height (H_{RZ}), were analyzed in Fig. 13, illustrating how W_{MP} and H_{RZ} evolve with linear energy (E_l) and hatch spacing (h_s). Measurements were taken from the consistently visible left half-width due to partial remelting by subsequent layers. The overlap ratio (τ_R) depends on W_{MP} and (h_s) . The overlap ratio τ_R depends on W_{MP} and h_s as follows:

$$\tau_R = 1 - (h_s/W_{MP}) \quad (4)$$

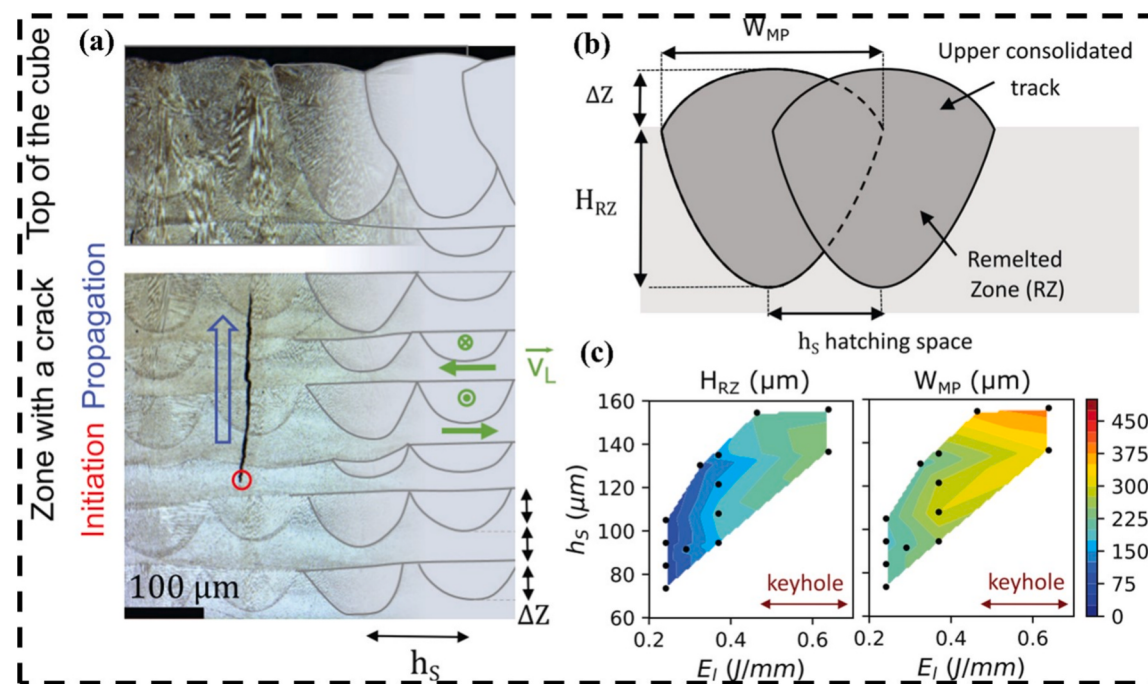


Fig. 13. (a) Initiation of a solidification crack transversely to the melt pool and propagation in higher layers; (b) Some geometrical features of melt pools; (c) Melt pool width W_{MP} and remelted zone height H_{RZ} as a function of linear energy $E_l = P/V_L$ and hatching space h_s (reproduced from Ref. [107] copyright 2020 Elsevier Ltd.).

The study revealed that larger melt pools increase microcracking due to extended mushy zones, while narrower melt pools with high overlap ratios reduce the occurrence of cracks. High overlap partially repairs existing cracks and narrows them, thereby minimizing propagation. Optimal parameters include low laser power, small hatch spacing, and a 90° scan rotation. Controlling melt pool size and overlap is crucial for producing dense, crack-free materials.

A comparative study was conducted to assess the influence of various scanning strategies on defect formation and mechanical properties in LPBF-formed K438 superalloys [119]. As illustrated in Fig. 14, schematics of the “back-and-forth” and island-type scanning strategies are presented. The results revealed that the island-type scanning strategy often initiates or terminates laser runs at overlap regions. The laser's acceleration or deceleration in these areas results in prolonged dwell time, which increases local heat input. This leads to deeper melt pools, hindering gas escape from the molten material. Consequently, overlapping sections exhibit higher micro-porosity compared to other regions of the fabricated part. The presence of these pores significantly reduces the overall density [85]. In contrast, the “back-and-forth” scanning strategy achieved a higher density of up to 99.34 %. This improvement is attributed to the strategy's unique characteristics: rotating the scan vector direction by 67° between layers promotes uniform heat flow and alternating melt pool formation, ensuring homogeneous temperature gradients and complete powder melting, thereby enhancing density [120].

Unlike previous studies, Kumar et al. [121] investigated the fabrication of parts with varying densities in LPBF-formed CM247LC by exclusively modulating the scan speed to regulate heat input. Experimental results revealed that high heat input during the process tended to induce solidification cracks of high density, as illustrated in Fig. 15. Because the scanning direction was perpendicular to the crack orientation, significant tensile stress (210 MPa) developed along the scan direction during solidification. Furthermore, by integrating model predictions with numerical analysis, the study identified optimal processing conditions at a scan speed of 1600 mm/s, corresponding to an extrapolated normalized energy density of $E^* \approx 8.7$. Under these conditions, a crack-free and dense CM247LC alloy with minimal stress was

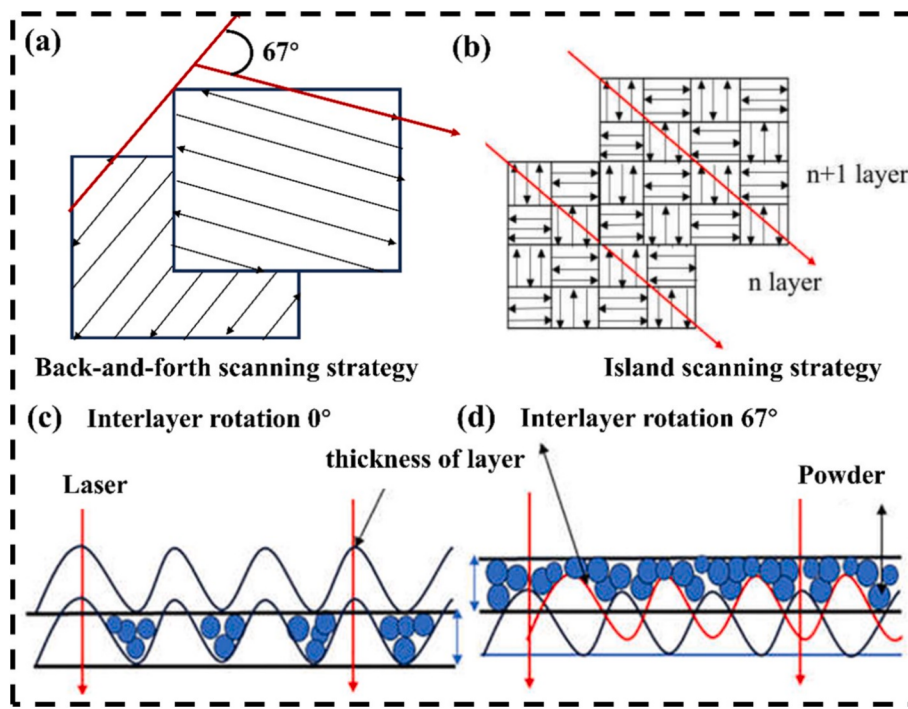


Fig. 14. Schematic diagram of scanning strategies: (a) 'back-and-forth' and (b) island scanning strategies. Schematic diagram of powder with different interlayer rotation angles under the same layer thickness, (c) island scanning remelting mode and (d) 'back-and-forth' scanning mode (reproduced from Ref. [119] under a Creative Commons Attribution 4.0 International License).

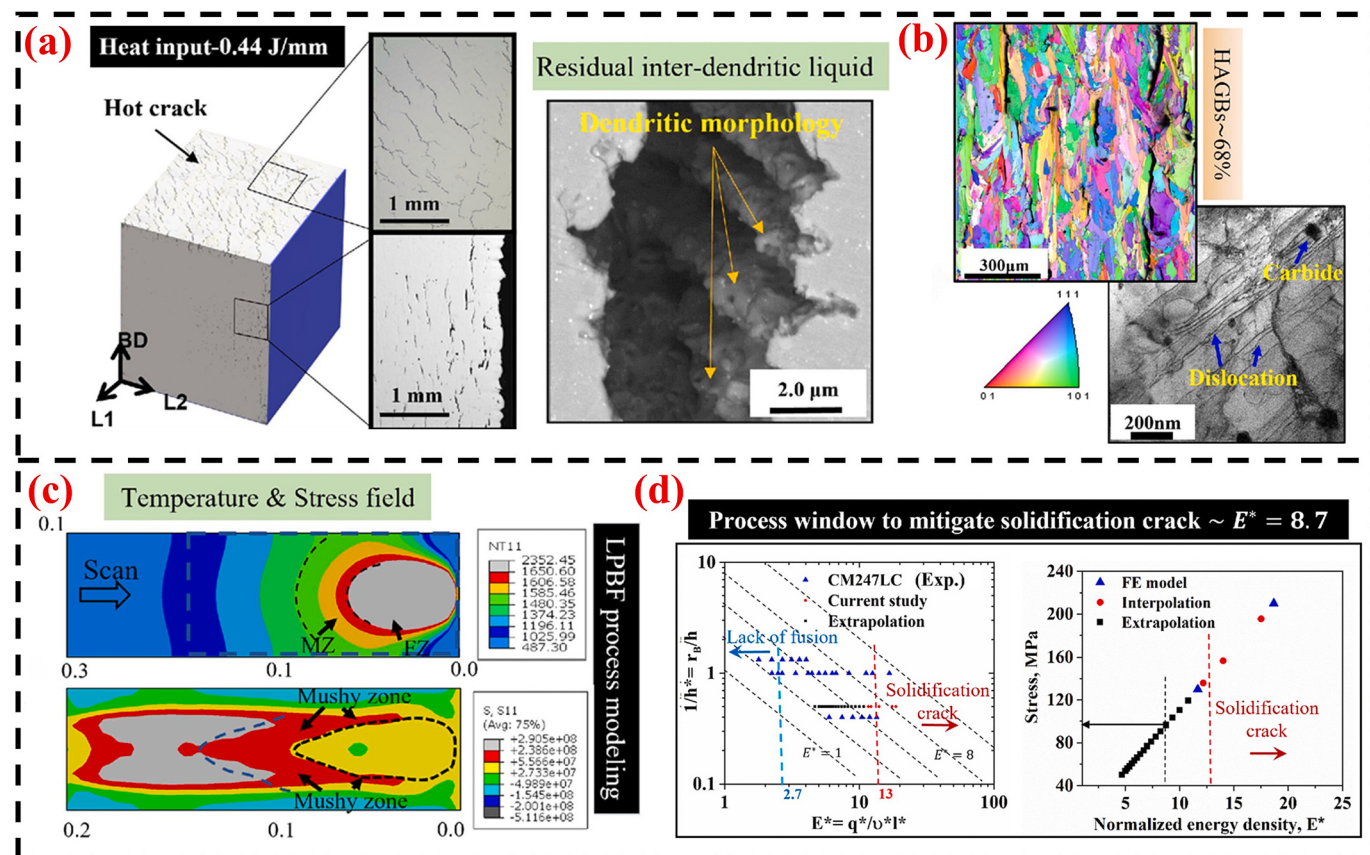


Fig. 15. Experimental characterization and simulation schematic diagram of LPBF-formed CM247LC: (a) Optical image of surface crack; (b) EBSD and TEM tests of sample; (c) Temperature and stress distribution contour map of simulated layer deposition;(d) Process window to determine optimal normalized energy density for defect-free CM247LC alloy (reproduced from Ref. [121] with permission from the Springer Nature).

achieved. The study also developed a mathematical model to describe the relationship between the solidification behavior of LPBF-formed CM247LC and scan speed, providing a practical framework for predicting other process parameters. Laser remelting in LPBF facilitates the production of CM247LC alloy parts with reduced crack density and enhanced performance. As illustrated in Fig. 16, different linear energy densities and remelting scan strategies [122] are classified into Parallel Remelting (PR) and Diagonal Remelting (DR). Research findings demonstrate that remelted samples exhibit reduced elemental segregation in regions previously affected by cracks. However, excessively high remelting energy densities can enlarge the melt pool, exacerbate grain misalignment at its edges, and increase susceptibility to cracking. In contrast, the Diagonal Remelting (DR) strategy reduces localized heat accumulation, minimizes thermal and stress gradients, and suppresses crack formation. Furthermore, remelting can eliminate unfused pores and mitigate elemental segregation. The authors suggest that optimizing remelting parameters ($P = 100$ W, $v = 1000$ mm/s, $hs = 40$ μm , scanning strategy = DR) can effectively suppress defects in LPBF-produced CM247LC components, significantly enhancing strength and ductility compared to non-remelted parts.

To optimize the LPBF-formed HWSA, Table 2 lists the optimization processes of processing parameters in the LPBF forming process and the corresponding results of performance changes for several typical HWSAs. Although some research has been conducted on LPBF for these alloys, numerous challenges persist. Key issues include the varying responses of different alloy compositions to processing conditions, as well as the intricate relationships between processing variables, microstructural features, and material properties. Different HWSA exhibit significant differences in response to process parameters. The complex parameter-microstructure-property relationships have not been fully clarified, which has hindered the promotion of the process. Future research can integrate machine learning to develop predictive models,

Table 2
Process optimization results for typical HWSA.

HWSA type	Key optimization parameters	Performance improvements
IN738LC	Low power, small scan spacing, 90° scan rotation	Crack density reduced, density > 99 %
K438 [119]	800–1200 mm/s round-trip scan + 67° interlayer rotation	Porosity reduced, density 99.34 %
CM247LC	1600 mm/s scanning speed + DR [121]	Crack-free, less segregation, better mechanics
Rene77 [4]	Bidirectional scan + 100 J/mm ² VED + heat treatment	Crack-free, high-temp performance enhanced
K418 [41]	1200 mm/s scanning speed	Enhancement of mechanical properties
ZGH451 [93]	low-power Gaussian laser	Improve the microhardness
René N5 [33]	1100/1300 W laser power	Improve the microhardness

uncover the adaptation laws between alloy compositions and process parameters, and realize the rapid migration of process windows across different HWSA. Additionally, further investigations should be conducted on the mechanism by which the coupling of multiple parameters (laser power, scanning speed, and scanning strategies) affects melt pool behavior (flow, thermal distribution) and microstructure evolution.

5. Heat treatment and properties of HWSA

Appropriate heat treatment can significantly enhance the corrosion resistance of specimens by reducing micro-segregation and altering the morphology of the second phase [123]. The heat treatment process for common HWSA typically involves solution treatment, aging treatment, and hot isostatic pressing (HIP). Solution treatment dissolves γ' particles in the matrix, eliminates micro-inhomogeneities formed during

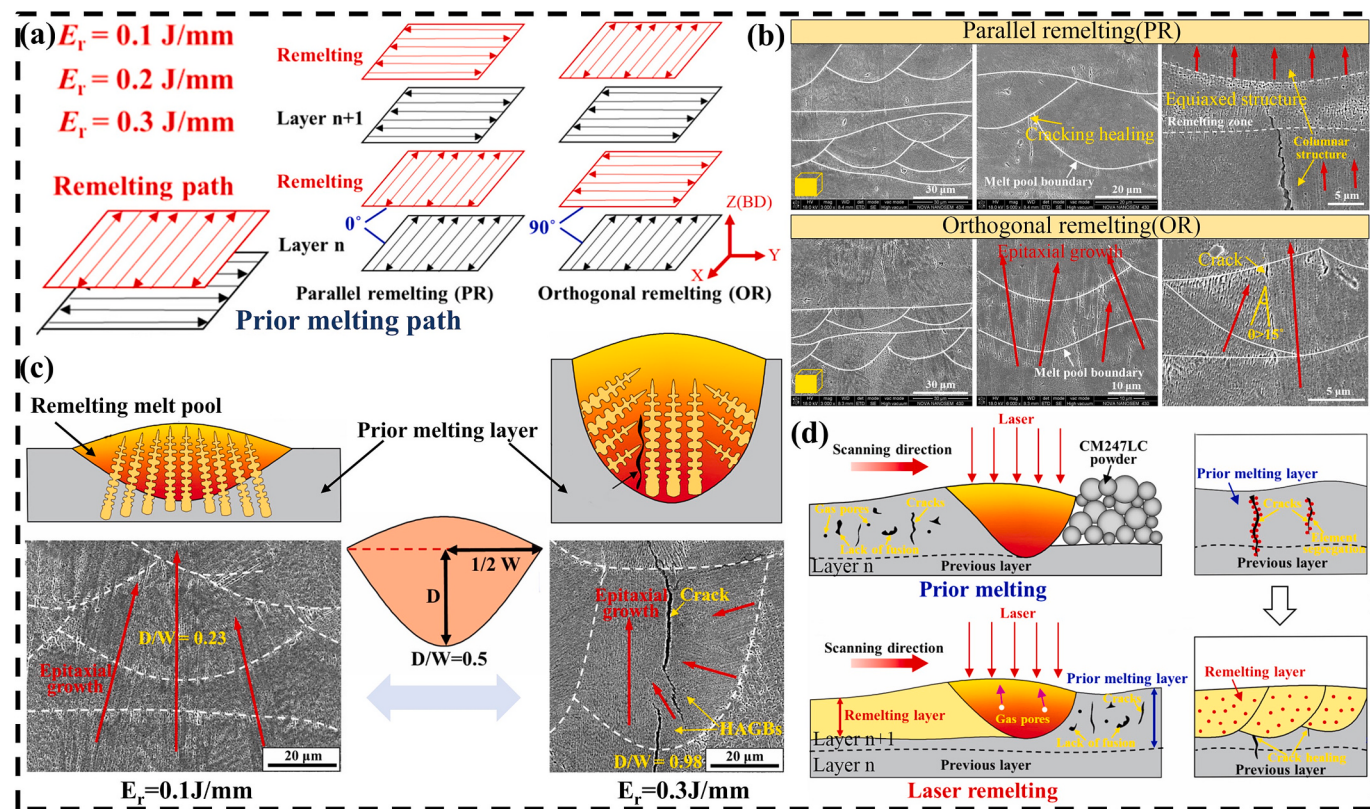


Fig. 16. LPBF-processed CM247LC samples: (a) linear energy density of remelting E_r and remelting scan strategies; (b) SEM micrographs with different remelting scan strategies; (c) The shape and size of melt pools with different energy density values of remelting; (d) Mechanism in the prior/ remelting process (adapted from Ref. [122] copyright 2021 Elsevier Ltd.).

processing, and homogenizes the alloy composition, thereby preparing for the material for subsequent aging treatment. This homogenization of the alloy composition enhances the plasticity and ductility of the fabricated parts. Aging treatment promotes the re-precipitation of dense, uniform, and optimally sized γ' particles within the matrix [74]. The primary objective is to enhance the strength and hardness of the alloy by precipitating strengthening phases. HIP subjects the alloy to elevated temperatures (1100–1200 °C) and high pressures (100–200 MPa) to eliminate internal pores and micro-cracks, thereby improving the alloy's density and mechanical properties.

LPBF-formed HWSA has microstructures featuring columnar grains, a γ -matrix, γ' precipitates, and brittle Laves phases. Compared to forged components, excessive segregation of Laves phases and insufficient γ'/γ'' precipitation compromise its mechanical properties. Post-heat treatments can dissolve Laves phases and optimize γ'/γ'' distribution, markedly boosting strength and creep resistance to meet aerospace criteria. Wang et al. [124] utilized LPBF to fabricate IN738LC turbine blades and evaluated various post-treatment methods (Table 3). They discovered that HIP improved tensile strength and elongation. SEM and XRD analyses revealed that γ' precipitates, which were absent in as-printed samples, formed after post-treatment, thereby enhancing mechanical properties. CT scans indicated minimal defects, with surface pores being removable through polishing. However, heat treatment alone did not yield improvements in properties. In fact, after SHT or DAHT, tensile strength slightly decreased (Fig. 17e). This decline may be attributed to grain coarsening during the heat treatment process. The optimal results were achieved with the combination of HIP and DAHT. Messé et al. [125] investigated post-treatment micro-precipitation and noted that metastable MC carbides formed due to the segregation of γ' -forming elements at cell boundaries. Stress-relief heat treatment adjusted the precipitated phases, which may help reduce stresses inherent to LPBF-formed materials.

Thermally induced precipitates play a crucial role in crack nucleation within additive-manufactured superalloys, significantly influencing their mechanical behavior. K438 specimens fabricated via LPBF undergo a sequential thermal regimen: solution treatment at 1120 °C for 2 h with air quenching, followed by aging at 850 °C for 24 h and subsequent cooling. Post-treatment microstructural analysis reveals the formation of $M_{23}C_6$ carbides through the interaction of Al, Ni, and Ti with the γ -matrix, resulting in banded microstructural features. These carbides exert dual influences: (1) dislocation pinning enhances yield strength by restricting plastic deformation, while (2) grain boundary segregation reduces interfacial ductility, promoting embrittlement. When applied stresses exceed the critical plasticity threshold of grain boundaries, intergranular crack propagation occurs. Concurrently, reduced grain misorientation and homogeneous dispersion of secondary γ' precipitates within the matrix [40] correlate with optimized mechanical properties, including a peak Young's modulus of 217.44 GPa and ultimate tensile strength of 1421.7 MPa. CM247LC, a nickel-based superalloy with a high γ' -phase volume fraction (~67 %), exhibits a pronounced susceptibility to thermally induced fracture during post-LPBF heat treatment. Boswell et al. [126] investigated temperature-dependent cracking mechanisms in this alloy, categorizing post-processing thermal regimes into two domains: 400–700 °C and

745–945 °C. Their findings reveal distinct fracture modes: DDC predominates at temperatures below 700 °C due to reduced grain boundary cohesion, while SAC dominates above 750 °C, driven by residual stress accumulation and precipitate coarsening. Mitigation strategies include parametric optimizing annealing cycles or implementing surface engineering interventions such as shot peening, which introduces compressive residual stresses to counteract tensile crack initiation. Notably, subcritical annealing (below 700 °C) partially alleviates process-induced stresses, enhancing component strength despite minor microcrack formation [127]. Complementary studies demonstrate that HIP at 1280 °C and 150 MPa for 2 h increases hardness by 8.2 % through pore elimination and γ' phase redistribution, underscoring the efficacy of HIP in microstructural refinement.

Heat treatment refines the grain structure, optimizes the distribution of the γ' phase, and eliminates internal defects resulting from the forming process, thereby enhancing mechanical properties. This process leads to increased tensile strength, hardness, corrosion resistance, and oxidation resistance. The careful selection of heat treatment parameters—including temperature, holding time, and cooling rate—is essential for achieving the desired microstructure. For LPBF-formed HWSA, appropriate heat treatments significantly improve material reliability and lifespan, facilitating the production of high-performance components. Future research should focus on further optimizing these processes to ensure an ideal alignment between microstructure and performance. Traditional heat treatment processes, such as single-step solution treatment and aging, often struggle to completely eliminate residual stresses and micro-defects resulting from the LPBF process. Therefore, it is crucial to develop composite heat treatment techniques, such as combining HIP with gradient aging treatment. Additionally, controlling grain orientation through methods like recrystallization induced by laser remelting should be implemented. This integrated approach aims to achieve several objectives: eliminating defects, refining the microstructure, and homogenizing material properties. To address this issue, it is essential to develop composite heat treatment technologies, such as combining HIP with gradient aging. Additionally, controlling grain orientation can be accomplished by inducing recrystallization through laser remelting. This integrated approach aims to eliminate defects, refine the microstructure, and achieve homogenization of material properties. For next-generation ultra-superalloys, developing low-temperature, short-duration heat treatment processes is also crucial for suppressing γ' phase coarsening and preventing the precipitation of harmful TCP phase precipitation.

Overall, the relationships among microstructural characteristics, post-processing methods, and performance control in LPBF of HWSA have been the subject of extensive research. The morphology, size, and type of microstructures significantly influence macroscopic properties; diverse microstructural features may emerge, and defects such as porosity and cracking can occur. To enhance performance, optimizing process parameters, scanning strategies, compositional adjustments, and post-processing techniques have effectively improved the alloy's mechanical properties and high-temperature resistance, including tensile strength and elongation. As summarized in Table 4, significant progress has been made in this area of research. However, the correlation mechanisms between microstructures and properties in HWSA with specific compositions remain inadequately understood.

This part focuses on the heat treatment of LPBF-formed HWSA and its influence on properties. The main heat treatment methods include solution treatment, aging treatment, HIP, and composite treatments. Their core functions involve dissolving harmful phases (Laves phases), optimizing the distribution of γ' phases, eliminating internal defects, and thereby enhancing mechanical properties. Research on the synergistic effect between grain refinement and γ' phase regulation, as well as the inhibition of γ' phase coarsening and the precipitation of topologically close-packed (TCP) phases, remains a key issue. Furthermore, to meet the requirements of next-generation ultra-high-temperature alloys, in addition to studies on traditional mechanical properties, it is necessary

Table 3
Post heat treatments for the as-printed or HIP samples of LPBF-formed IN738LC.

Type of post heat treatment	HIP	Post heat treatment details
Standard	None	1120 °C/2h/AC + 850 °C/24 h
Double aging	None	1120 °C/2h/AC + 1055 °C/1h + 850 °C/24 h
HIP and Standard	1175 °C/100 MPa/4h	1120 °C/2h/AC + 850 °C/24 h
HIP and double aging	1175 °C/100 MPa/4h	1120 °C/2h/AC + 1055 °C/1h + 850 °C/24 h

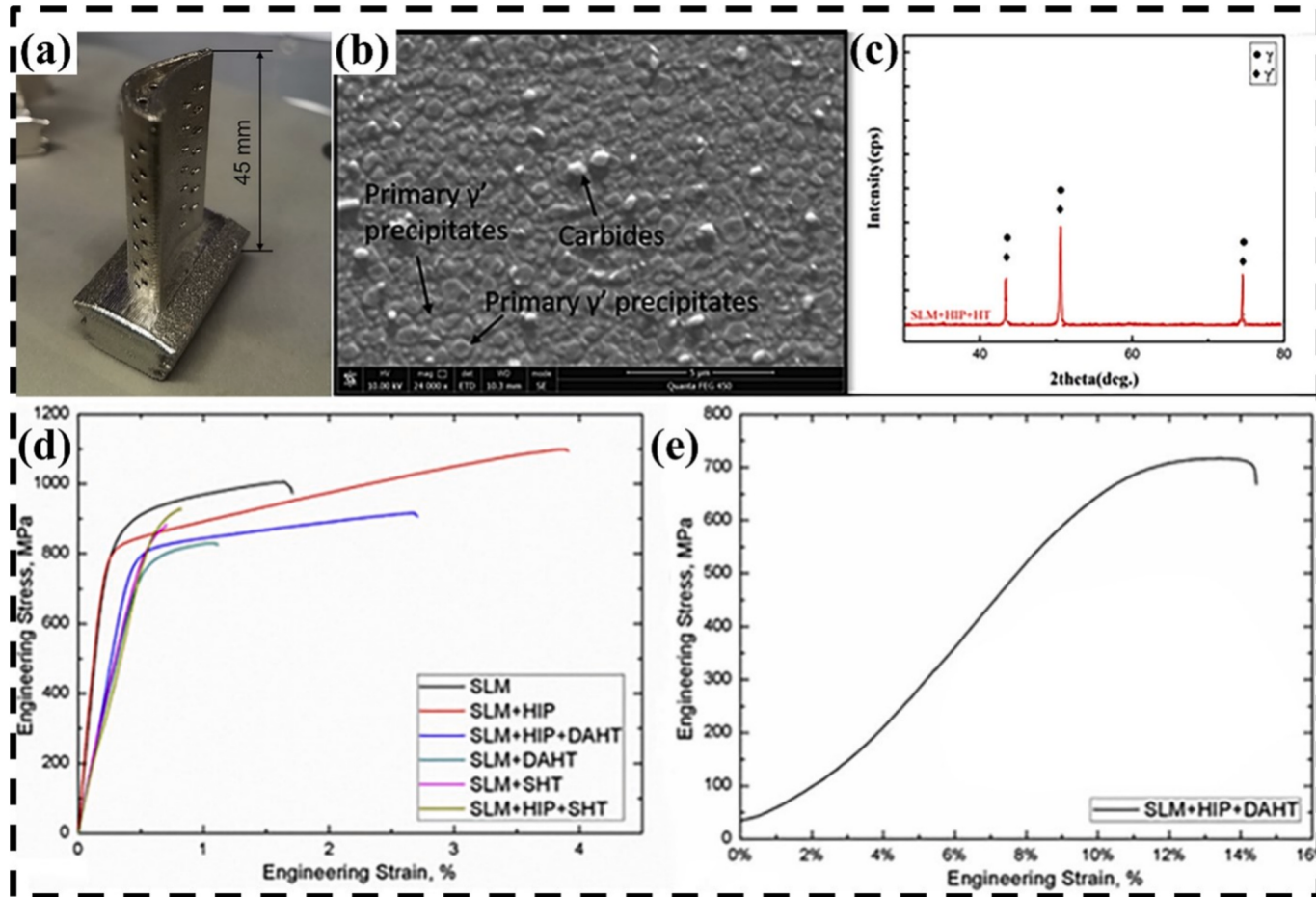


Fig. 17. Microscopic characterization and macroscopic properties of LPBF-formed IN738LC: (a) Camera snapshot of a jet turbine blade fabricated by LPBF; Showing γ , γ' and carbide phases in the microstructure in (b) and (c) XRD result for IN738LC; (d) Tensile curves of different samples of the as-printed (adapted from Ref. [123] copyright 2019 Elsevier Ltd.).

Table 4
Common LPBF-formed HWSA of microstructure characteristics and performance.

Ref.	Materials	Density	Microstructure	Performance	Method
[31]	CMSX-4	Cracks-free	Reduce the γ phase's size + uniformity	Durability from 240 to 356 h	Heat-treatment process
[41,61]	K418	97.80 %	γ'/γ'' phase increasing + crystal structure change	Mechanical property enhancement	200 W laser power
[66,107]	IN738	99.46 %	Grain number increasing and average grain diameter decreasing	$YS-h = 1049.4 \pm 21.1$ MPa, $EL-h = 21.1 \pm 0.8$ %	Scanning strategy; Heat treatment
[71]	IN738	Cracks porosity (<0.4 %)	Reduction of γ/γ' eutectics	$EL = 9-14.7$ %, $UTS = 1320-1598$ MPa	C element change
[93]	ZGH451	99.90 %	$<1 \mu m$ MC-type carbides + no harmful γ/γ' eutectic	Mechanical property enhancement	Directional solidification
[119]	K438	99.34 %	Reduce the anisotropy + carbides type change	Excellent mechanical properties	scan strategy + Heat treatment
[121,122]	CM247LC	Low Cracks	Cracks propagate + high-stress concentration	$UTS = 1280$ MPa, $YS = 885$ MPa, $EL = 11.9$ %	Remelting parameters + strategy

to conduct tests on high-temperature wear resistance, corrosion resistance, and impact resistance [39,131], so as to align with the actual service conditions of HWSA.

6. Conclusions and Outlooks

This review systematically analyzes existing studies on LPBF-formed HWSA, focusing on microstructural precipitation characteristics, optimization of process parameters and scanning strategies, defect suppression mechanisms, and post-processing enhancements. The goal is to explore the potential of LPBF technology in manufacturing high-quality, high-performance HWSA aerospace hot-end components. Key findings

are summarized as follows:

- Owing to the layered fabrication characteristic of LPBF, the cooling rate decreases as height increases along the deposition direction, leading to microstructural inhomogeneity: grains in the upper layers are coarser, whereas those in the lower layers are finer. This inhomogeneity further induces mechanical property anisotropy. The type of grains (columnar/equiaxed) is determined by the ratio of G to solidification rate R, and can be regulated through means such as optimization of scanning strategies.
- In terms of precipitated phases, strengthening phases such as γ , γ'' phases and carbides like MC are crucial for the performance of LPBF-

- formed HWSA, while harmful phases such as Laves and η phases reduce plasticity and increase crack sensitivity.
- Pore defects include lack-of-fusion pores (formed due to insufficient powder melting and gas entrapment) and keyhole pores (induced by high laser energy density). Porosity can be reduced by optimizing process parameters or adjusting compositions (adding carbon), but it is difficult to completely avoid cracks.
 - Solidification cracks originate from the shrinkage stress in the mushy zone during the final stage of solidification, which breaks the interdendritic liquid film and propagates along high-angle grain boundaries. Liquation cracks are related to the formation of low-melting-point eutectic phases caused by elemental segregation (enrichment of Al and Ti), and cracks along grain boundary liquid films under thermal stress. Crack control can be achieved by regulating VED, optimizing scanning strategies, and adjusting compositions (controlling Al/Ti content, adding carbon).
 - Process parameters vary significantly in LPBF processing of different HWSA, and no universal optimization model exists. Scanning strategies influence density: “back-and-forth” scanning (with a 67° interlayer rotation) increases density to 99.34 % via uniform heat flow, whereas island scanning tends to induce more pores due to excessive local heat input. Melt pool size and overlap ratio correlate with crack formation, with narrow melt pools and high overlap ratios mitigating cracks. Scanning speed regulates heat input; remelting strategies (diagonal remelting) can reduce elemental segregation and defects. $M_{23}C_6$ carbides formed post-heat treatment exhibit both strengthening and embrittling effects; however, traditional heat treatment fails to fully eliminate residual stress and tends to induce precipitation of harmful topologically close-packed (TCP) phases.

The above summary clearly outlines the core issues in LPBF-formed HWSA across microstructural characteristics, precipitated phases, defect formation, process responsiveness, and heat treatment. These include performance anisotropy induced by microstructural inhomogeneity, reduced plasticity and heightened crack sensitivity caused by harmful phases, the difficulty in fully eradicating defects like pores and cracks, significant discrepancies in process parameter adaptability, and the limitations of traditional heat treatment methods. Collectively, these issues constitute the primary bottlenecks hindering the widespread adoption of the process and improvements in material performance within this field. To tackle these bottlenecks, future research directions have been proposed spanning material design [49], process optimization [122], beam shaping [128], monitoring and control [50,129], mechanistic exploration [130], and performance expansion [39,131]. This provides a systematic solution framework to overcome existing constraints and advance the in-depth application of LPBF technology in the domain of HWSA (Fig. 18).

- Ceramic particle reinforced composites for HWSA. LPBF of metal matrix composites (MMCs) with ceramic reinforcements helps refine microstructures, enhance interface bonding, reduce defects, and significantly improve composite mechanical properties. Most LPBF-fabricated composites with ceramic reinforcements currently use aluminum-based or iron-based matrices. This approach—breaking away from traditional chemical element regulation—can serve as a reference for LPBF processing of ceramic particle composites in hard-to-weld high-temperature alloys. Key future research will focus on strengthening mechanisms and interface reactions.
- Multi-physical scale simulation. HWSA is prone to cracks due to solute segregation and thermal stress concentration in LPBF. Multi-physical scale simulation through micro-meso-macro coupling can avoid the continuous trial-and-error of traditional experiments. Future research will focus on revealing defect formation mechanisms from a theoretical perspective and inhibiting defects through simulation.

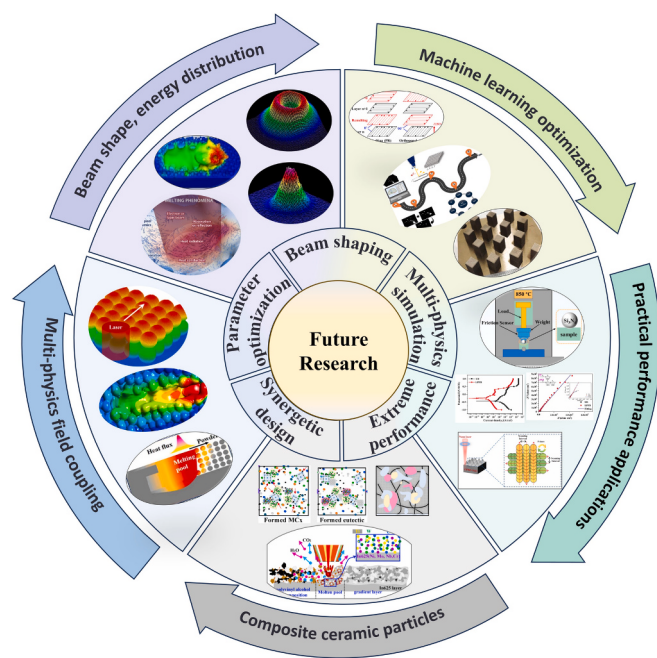


Fig. 18. Diagram of future research prospects for HWSA processed by LPBF (reproduced from Ref. [39] copyright 2024 Elsevier Ltd.; reproduced from Ref. [49] copyright 2025 Elsevier Ltd.; reproduced from Ref. [50] under a Creative Commons Attribution-Noncommercial License; reproduced from Ref. [122] copyright 2024 Elsevier Ltd.; reproduced from Ref. [128] copyright 2023 Elsevier Ltd.; reproduced from Ref. [129,130] copyright 2025 Elsevier Ltd.; reproduced from Ref. [131] copyright 2025 Elsevier Ltd.).

- Beam shaping combined with in-situ monitoring. In the process of LPBF-formed HWSA, concentrated laser energy tends to cause local overheating, leading to pores or thermal cracks. Beam shaping reduces temperature gradients and thermal stress in the melt pool by controlling energy density gradients; it also minimizes pores from rapid solidification, while inhibiting grain boundary segregation and precipitation of low-melting-point phases, thereby reducing solidification cracks. When combined with in-situ monitoring, this approach enables adaptive adjustment of laser energy to mitigate microstructural inhomogeneity.
- Parameter optimization combined with machine learning. To address non-equilibrium solidification in HWSA, combining machine learning with melt pool data collection enables adjustment of laser parameters, identification of optimal energy density ranges, and inhibition of elemental segregation and thermal cracks. This approach can overcome the limitations of traditional trial-and-error methods and efficiently map complex process windows.
- Performance characterization under extreme working conditions. LPBF-formed HWSA is used in aerospace hot-end components. Beyond traditional high-strength requirements, actual service conditions demand properties such as wear and corrosion resistance. Future research should expand testing of high-temperature wear resistance, corrosion resistance, and impact resistance under extreme service conditions to further extend their service life.

CRediT authorship contribution statement

Hang You: Writing – review & editing, Writing – original draft.
Guang Fu: Writing – review & editing. **Shangkun Jin:** Data curation.
Shengliang Luo: Funding acquisition. **Kaifei Zhang:** Validation. **Zhi-hao Ren:** Investigation. **Taiqian Mo:** Project administration. **Zhengwen Zhang:** Data curation.

Declaration of competing interest

The authors declare that they have no known competing financial interests or personal relationships that could have appeared to influence the work reported in this paper.

Acknowledgements

This work was funded by Guizhou Provincial Science and Technology Foundation of China (ZD [2025]083, BQW [2024]011, [2025] general 041, ZK [2023]078; Guizhou University Fund Project (China [2024]14; [2024]03).

Data availability

No data was used for the research described in the article.

References

- [1] N. Erdogan, A. Basigit, Investigating thermal shock and corrosion resistance of Inconel 601 super alloy after thermal barrier coating with %8 YSZ powder, Mater. Today Commun. 36 (2023) 106516, <https://doi.org/10.1016/j.mtcomm.2023.106516>.
- [2] M. Waeytens, A. Syed, T. Roberts, et al., A microscopy study of nickel-based superalloys performance in type I hot corrosion conditions, Mater. High Temp. 40 (4) (2023) 272–282, <https://doi.org/10.1080/09603409.2023.2188355>.
- [3] Y. Mu, Y. Liang, J. Sheng, et al., A novel approach to coating for improving the comprehensive high-temperature service performance of TiAl alloys, Acta Mater. (283) (2025) 120500, <https://doi.org/10.1016/j.actamat.2024.120500>.
- [4] M. Phan, D. Fraser, S. Gulizia, et al., Mechanism of hot crack propagation and prevention of crack formation during electron beam powder bed fusion of a difficult-to-weld Co-Cr-Ni-W superalloy, J. Mater. Process. Technol. 293 (2021) 117088, <https://doi.org/10.1016/j.jmatprotec.2021.117088>.
- [5] F. Xu, V. Dhokia, P. Colegrave, et al., Realisation of a multi-sensor framework for process monitoring of the wire arc additive manufacturing in producing Ti-6Al-4V parts, Int. J. Comput. Integr. Manuf. 31 (8) (2018) 785–798, <https://doi.org/10.1080/0951192X.2018.1466395>.
- [6] R. Jiang, Y. Yang, H. Wang, et al., Improving overlapping quality of 316L stainless steel fabricated by multi-laser powder bed fusion through optimizing non-remelting scanning strategy, J. Manuf. Process. 145 (2025) 333–345, <https://doi.org/10.1016/j.jmapro.2025.04.071>.
- [7] J. Wang, D. Yuan, X. Sun, et al., Effect of deposition sequence on interface characteristics of IN718/CuSn10 horizontal bimetallic structures via laser directed energy deposition, Mater. Des. 255 (2025) 114085, <https://doi.org/10.1016/j.matdes.2025.114085>.
- [8] P. Baranowski, P. Platek, A. Dudka, et al., Deformation of honeycomb cellular structures manufactured with Laser Engineered Net Shaping (LENS) technology under quasi-static loading: Experimental testing and simulation, Addit. Manuf. 25 (2019) 307–316, <https://doi.org/10.1016/j.addma.2018.11.018>.
- [9] L. Quinonez, A. Liévano, A. Hernández, et al., Synthesis and characterization of semi-transparent gehlenite ceramic spheres obtained by selective laser sintering, Bol. Soc. Mex. Hist. Filos. Med. 64 (1) (2025) 21–32, <https://doi.org/10.1016/j.bsecv.2024.09.004>.
- [10] M. Dogu, E. Carthy, R. Cann, et al., Digitisation of metal AM for part microstructure and property control, Int. J. Mater. Form. 15 (3) (2022), <https://doi.org/10.1007/s12289-022-01686-4>.
- [11] R. Joshua, S. Raj, M. Sultan, et al., Powder Bed Fusion 3D Printing in Precision Manufacturing for Biomedical Applications: A Comprehensive Review, Materials 17(3) (2024) ma17030769, <https://doi.org/10.3390/ma17030769>.
- [12] S. Narasimharaju, W. Zeng, T. See, et al., A comprehensive review on laser powder bed fusion of steels: Processing, microstructure, defects and control methods, mechanical properties, current challenges and future trends, J. Manuf. Process. 75 (2022) 375–414, <https://doi.org/10.1016/j.jmapro.2021.12.033>.
- [13] E. Sefene, State-of-the-art of selective laser melting process: a comprehensive review, J. Manuf. Syst. 63 (2022) 250–274, <https://doi.org/10.1016/j.jmsy.2022.04.002>.
- [14] Y. Wu, K. Sun, S. Yu, et al., Modeling the selective laser melting-based additive manufacturing of thermoelectric powders, Addit. Manuf. 37 (2021) 101666, <https://doi.org/10.1016/j.addma.2020.101666>.
- [15] O. Adegoke, J. Andersson, H. Brodin, et al., Review of Laser Powder Bed Fusion of Gamma-Prime-Strengthened Nickel-Based Superalloys, Metals. 10(8) (2020) 996, <https://doi.org/10.3390/met10080996>.
- [16] G. Zhu, D. Kong, W. Zhou, et al., Research progress on the crack formation mechanism and cracking-free design of γ' phase strengthened nickel-based superalloys Fabricated by Selective Laser Melting, Acta Metall. Sin. 59 (1) (2023) 16–30, <https://www.ams.org.cn/EN/10.11900/0412.1961.2022.00434>.
- [17] G. Bryndza, J. Tchuindjang, F. Chen, et al., Review of the Microstructural Impact on Creep Mechanisms and Performance for Laser Powder Bed Fusion Inconel 718, Materials 18(2) (2025) 276, <https://doi.org/10.3390/ma18020276>.
- [18] C. Jiang, Masrurotin, A. Wibisono, et al., Enhancing Internal Cooling Channel Design in Inconel 718 Turbine Blades via Laser Powder Bed Fusion: A Comprehensive Review of Surface Topography Enhancements, Int. J. Precis. Eng. Manuf. 26(2) (2025) 487–511, <https://doi.org/10.1007/s12541-024-01177-3>.
- [19] K. Li, J. Zhan, Y. Wang, et al., Application of data-driven methods for laser powder bed fusion of Ni-based superalloys: a review, J. Manuf. Process. 133 (2025) 285–321, <https://doi.org/10.1016/j.jmapro.2024.11.053>.
- [20] M. Karmuhilan, S. Kumanan, A review on additive manufacturing processes of inconel 625, J. Mater. Eng. Perform. 31 (4) (2022) 2583–2592, <https://doi.org/10.1007/s11665-021-06427-3>.
- [21] D. Srinivasan, K. Ananth, Recent advances in alloy development for metal additive manufacturing in gas turbine/aerospace applications: a review, J. Indian Inst. Sci. 102 (1) (2022) 311–349, <https://doi.org/10.1007/s41745-022-00290-4>.
- [22] K. Li, Z. Zhu, B. Xiao, et al., State of the art overview material degradation in high-temperature supercritical CO₂ environments, Prog. Mater Sci. 136 (2023) 101107, <https://doi.org/10.1016/j.pmatsci.2023.101107>.
- [23] D. Lin, X. Xi, M. Yan, et al., Significantly improved weldability in laser welding of additively manufactured haynes 230 superalloys by tailoring microstructure, J. Mater. Res. Technol. 26 (2023) 7873–7892, <https://doi.org/10.1016/j.jmrt.2023.09.134>.
- [24] A. Ramakrishnan, G. Dinda, Microstructure and mechanical properties of direct laser metal deposited Haynes 282 superalloy, Mater. Sci. Eng., A 748 (2019) 347–356, <https://doi.org/10.1016/j.msea.2019.01.101>.
- [25] T. Shi, J. Li, G. Gao, et al., Microstructural evolution and formation of fine grains during fatigue crack initiation process of laser powder bed fusion Ni-based superalloy, Addit. Manuf. 85 (2024) 104151, <https://doi.org/10.1016/j.addma.2024.104151>.
- [26] A. Banerjee, M. He, W. Musinski, et al., Effect of stress-relief heat treatments on the microstructure and mechanical response of additively manufactured IN625 thin-walled elements, Mater. Sci. Eng., A 846 (2022) 143288, <https://doi.org/10.1016/j.msea.2022.143288>.
- [27] A. Paraschiv, G. Matache, M. Vladut, Assessment of residual stresses in laser powder bed fusion manufactured IN 625, Materials 17 (2) (2024) 413, <https://doi.org/10.3390/mat17020413>.
- [28] Z. Liu, S. Xin, Y. Zhao, Research progress on the creep resistance of high-temperature titanium alloys, A Review, Metals. 13 (12) (2023) 1975, <https://doi.org/10.3390/met13121975>.
- [29] A. Gloria, R. Montanari, M. Richetta, et al., Alloys for aeronautic applications: state of the art and perspectives, Metals 9 (6) (2019) 662, <https://doi.org/10.3390/met9060662>.
- [30] M. Grilli, D. Valerini, A. Slobozeanu, et al., Critical raw materials saving by protective coatings under extreme conditions: a review of last trends in alloys and coatings for aerospace engine applications, Materials 14 (7) (2021) 1656, <https://doi.org/10.3390/ma14071656>.
- [31] A. Basak, S. Raghu, S. Das, Microstructures and microhardness properties of CMSX-4® additively fabricated through scanning laser epitaxy (SLE), J. Mater Eng Perform 26 (2017) 5877–5884.
- [32] R. Wang, J. Wang, T. Cao, et al., Microstructure characteristics of a René N5 Ni-based single-crystal superalloy prepared by laser-directed energy deposition, Addit. Manuf. 61 (2023) 103363, [https://doi.org/10.1016/j.addma.2022.103363Get rights and content](https://doi.org/10.1016/j.addma.2022.103363).
- [33] K. Jahns, R. Bappert, P. Bhlke, et al., Additive manufacturing of CuCr1Zr by development of a gas atomization and laser powder bed fusion routine, Int. J. Adv. Manuf. Technol. 107 (2020) 2151–2161, <https://doi.org/10.1007/s00170-020-04941-7>.
- [34] P. Wang, J. Liang, Y. Zhu, et al., Pursued strength-ductility synergy in Ni superalloys produced by laser powder bed fusion: Crystallographic lamellar versus Directionally solidified microstructure, Mater. Sci. Eng., A 925 (2025) 147838, <https://doi.org/10.1016/j.msea.2025.147838>.
- [35] H. Zhang, Q. Han, Z. Zhang, et al., Combined effects of carbon content and heat treatment on the high-temperature tensile performance of modified IN738 alloy processed by laser powder bed fusion, Mater. Sci. Eng., A 920 (2025) 147538, <https://doi.org/10.1016/j.msea.2024.147538>.
- [36] R. Raghu, P. Chandramohan, D. Kumar, et al., Structural characterization and strength assessment of laser powder bed fusion manufactured CM247LC nickel based super alloy, J. Mater. Eng. Perform. 32 (2023) 11310–11325, <https://doi.org/10.1007/s11665-023-08550-9>.
- [37] M. Abdelwahed, J. Puchades, L. Grinán, et al., Cracking mechanisms and effect of extensive preheating in CM247LC and IN713LC Ni-base superalloy processed by Laser Powder Bed Fusion, Mater. Today Commun. 37 (2023) 107644, <https://doi.org/10.1016/j.mtcomm.2023.107644>.
- [38] M. Hafezi, A. Kermanpur, A. Rezaeian, et al., Investigating crack formation in IN738LC Ni-based superalloy fabricated by laser powder-bed fusion process, J. Mater. Res. Technol. 29 (2024) 1983–2002, <https://doi.org/10.1016/j.jmrt.2024.01.264>.
- [39] Y. Hu, X. Zhang, H. Jia, et al., High-temperature fretting wear behavior of IN738LC alloy formed by laser powder bed fusion, Tribol. Int. 199 (2024) 110017, <https://doi.org/10.1016/j.triboint.2024.110017>.
- [40] X. Xie, F. Zhang, C. Peng, et al., Effect of scan strategy and substrate preheating on crack formation in IN738LC Ni-based superalloy during laser powder bed fusion, Mater Charact 221 (2025) 114722, <https://doi.org/10.1016/j.matchar.2025.114722>.
- [41] Y. Lu, Y. Zhou, P. Wen, et al., Effect of laser power on microstructure and mechanical properties of K418 nickel-based alloy prepared by selective laser melting, J. Mater. Res. Technol. 27 (2023) 2964–2975, <https://doi.org/10.1016/j.jmrt.2023.10.189>.

- [42] M. Tinat, M. Uddagiri, I. Steinbach, et al., Numerical simulations to predict the melt pool dynamics and heat transfer during single-track laser melting of Ni-based superalloy (CMSX-4), *Metals* 13 (6) (2023) 1091, <https://doi.org/10.3390/met13061091>.
- [43] J. Lu, X. Liu, Y. Zhu, et al., Thermal-mechanical behavior of LPBF GH3536 superalloy using in-situ SEM tensile, *Eng. Fail. Anal.* 173 (2025) 109423, <https://doi.org/10.1016/j.engfailanal.2025.109423>.
- [44] A. Basak, Additive Manufacturing of High-Gamma Prime Nickel-Based Superalloys through Selective Laser Melting (SLM), *Solid Freeform Fabrication 2019, Proceedings of the 30th Annual International* (2019), <https://doi.org/10.26153/tsw/17293>.
- [45] S. Ozer, M. Doğu, C. Ozdemirel, et al., Effect of aging treatment on the microstructure, cracking type and crystallographic texture of IN939 fabricated by powder bed fusion-laser beam, *J. Mater. Res. Technol.* 33 (2024) 574–588, <https://doi.org/10.1016/j.jmrt.2024.09.106>.
- [46] D. Raabe, M. Herbig, S. Sandlöbes, et al., Grain boundary segregation engineering in metallic alloys: a pathway to the design of interfaces, *Curr. Opin. Solid State Mater. Sci.* 18 (4) (2014) 253–261, <https://doi.org/10.1016/j.cossm.2014.06.002>.
- [47] M. Phan, O. Dew, I. Todd, Predictive process diagram for parameters selection in laser powder bed fusion to achieve high-density and low-cracking built parts, *Addit. Manuf.* 85 (2024) 104145, <https://doi.org/10.1016/j.addma.2024.104145>.
- [48] C. Formanoir, M. Nasab, L. Schlinger, et al., Healing of keyhole porosity by means of defocused laser beam remelting: Operando observation by X-ray imaging and acoustic emission-based detection, *Addit. Manuf.* 79 (2024) 103880, <https://doi.org/10.1016/j.addma.2023.103880>.
- [49] W. Zu, A. Li, M. Zhao, et al., Microstructure and properties behavior of in situ synthesized with high content (Ti, W) C reinforced In625 by two step-laser direct energy deposition, *Opt. Laser Technol.* 181 (2025) 111982, <https://doi.org/10.1016/j.optlastec.2024.111982>.
- [50] P. Akbari, M. Zamani, A. Mostafaei, Machine learning predictions of spatter behavior in LPBF Additive Manufacturing, *Materialia* 38 (2024) 102268, <https://doi.org/10.1016/j.mtla.2024.102268>.
- [51] J. Ruiz, F. Galbusera, L. Caprio, et al., Laser beam shaping facilitates tailoring the mechanical properties of IN718 during powder bed fusion, *J. Mater. Process. Technol.* 328 (2024) 118393, <https://doi.org/10.1016/j.jmatprote.2024.118393>.
- [52] H. Hamdi, H. Abedi, Thermal stability of Ni-based superalloys fabricated through additive manufacturing: a review, *J. Mater. Res. Technol.* 30 (2024) 4424–4476, <https://doi.org/10.1016/j.jmrt.2024.04.161>.
- [53] M. Kuntoglu, E. Salur, M. Gupta, et al., A review on microstructure, mechanical behavior and post processing of additively manufactured Ni-based superalloys, *Rapid Prototyp. J.* 30 (9) (2024) 1890–1910, <https://doi.org/10.1108/RPJ-10-2023-0380>.
- [54] S. Sanchez, P. Smith, Z. Xu, et al., Powder Bed Fusion of nickel-based superalloys: a review, *Int. J. Mach. Tools Manuf.* 165 (2021) 103729, <https://doi.org/10.1016/j.ijmachtools.2021.103729>.
- [55] A. Dwivedi, M. Khurana, Y. Bala, et al., Effect of heat treatment on microstructure and mechanical properties for laser powder bed fusion of nickel-based superalloy: a review, *Mater. Today Proc.* 115 (2024) 280–288, <https://doi.org/10.1016/j.matpr.2023.09.093>.
- [56] Z. Hao, T. Tian, X. Li, et al., Effects of hot processes on microstructure evolution and tensile properties of FGH4096 Ni-based superalloy processed by Laser Powder Bed Fusion, *Mater. Sci. Eng., A* 804(2021)140775, <https://doi.org/10.1016/j.msea.2021.140775>.
- [57] O. Bologna, S. Cecchel, G. Cornacchia, et al., Investigating post-processing impact on fatigue performance of LPBF Ti6Al4V with heat treatment, high pressure heat treatment, and dry electropolishing strategies, *Int. J. Fatigue* 185 (2024) 108365, <https://doi.org/10.1016/j.ijfatigue.2024.108365>.
- [58] M. Hasanalbadi, S. Shahabad, A. Keshavarzkermani, et al., A numerical modelling for laser Powder-bed fusion of Ti-alloy with a hybrid heat source: an investigation on solidification and microstructure formation, *Opt. Laser Technol.* 174 (2024) 110647, <https://doi.org/10.1016/j.optlastec.2024.110647>.
- [59] N. Adomako, N. Haghbadi, S. Primig, Electron and laser-based additive manufacturing of Ni-based superalloys: a review of heterogeneities in microstructure and mechanical properties, *Mater. Des.* 223 (2022) 111245, <https://doi.org/10.1016/j.matdes.2022.111245>.
- [60] J. Fang, Y. Tan, E. Wei, et al., Effect of scanning speed on microstructure, mechanical, and tribological properties of SiC/Ti composites via laser powder bed fusion, *Opt. Laser Technol.* 192,Part A(2025)113444, <https://doi.org/10.1016/j.optlastec.2025.113444>.
- [61] W. Pei, C. Yi, C. Zhen, et al., Effect of heat treatment on microstructure and mechanical properties of K418 superalloy prepared by laser powder bed fusion, *Adv. Eng. Mater.* 27 (10) (2025), <https://doi.org/10.1002/adem.202403067>.
- [62] Yongqiang Y., Wang D., Selective Laser Melting 3D Printing Technology[M]. Huazhong University of Science and Technology Press, WuHan,2019.3.
- [63] M. Shahwaz, P. Nath, I. Sen, A critical review on the microstructure and mechanical properties correlation of additively manufactured nickel-based superalloys, *J. Alloys Compd.* 907 (2022) 164530, <https://doi.org/10.1016/j.jallcom.2022.164530>.
- [64] P. Wang, Y. Zhu, N. Lu, et al., Controllable period of crystallographic lamellar microstructure in ZGH451 superalloy prepared by laser powder bed fusion, *J. Mater. Sci. Technol.* 211 (2025) 239–243, <https://doi.org/10.1016/j.jmst.2024.06.008>.
- [65] M. Gäumann, C. Bezençon, P. Canalis, et al., Single-crystal laser deposition of superalloys: processing-microstructure maps, *Acta Mater.* 49 (6) (2001) 1051–1062, [https://doi.org/10.1016/S1359-6454\(00\)00367-0](https://doi.org/10.1016/S1359-6454(00)00367-0).
- [66] J. Xu, Y. Ding, Y. Gao, et al., Grain refinement and crack inhibition of hard-to-weld Inconel 738 alloy by altering the scanning strategy during selective laser melting, *Mater. Des.* 209 (2021) 109940, <https://doi.org/10.1016/j.matdes.2021.109940>.
- [67] R. Moreno, V. Divya, S. Driver, et al., Effect of heat treatment on the microstructure, texture and elastic anisotropy of the nickel-based superalloy CM247LC processed by selective laser melting, *Mater. Sci. Eng., A* 674(2016)529-539, <https://doi.org/10.1016/j.msea.2016.06.075>.
- [68] H. Yan, G. Zhu, H. Shi, et al., Microstructure and mechanical properties of K438 alloy processed by selective laser melting and subsequent heat treatment, *Mater. Charact.* 191 (2022) 112116, <https://doi.org/10.1016/j.matchar.2022.112116>.
- [69] T. Voisin, J. Forien, A. Perron, et al., New insights on cellular structures strengthening mechanisms and thermal stability of an austenitic stainless steel fabricated by laser powder-bed-fusion, *Acta Mater.* 203 (2021) 116476, <https://doi.org/10.1016/j.actamat.2020.11.018>.
- [70] X. Wang, L. Carter, B. Pang, et al., Microstructure and yield strength of SLM-fabricated CM247LC Ni-Superally, *Acta Mater.* 128 (2017) 87–95, <https://doi.org/10.1016/j.actamat.2017.02.007>.
- [71] W. Zhou, Y. Tian, Q. Tan, et al., Effect of carbon content on the microstructure, tensile properties and cracking susceptibility of IN738 superalloy processed by laser powder bed fusion, *Addit. Manuf.* 58 (2022) 103016, <https://doi.org/10.1016/j.addma.2022.103016>.
- [72] J. Xu, Z. Huang, L. Jiang, Effect of heat treatment on low cycle fatigue of IN718 superalloy at the elevated temperatures, *Mater. Sci. Eng., A* 690 (2017) 137–145, <https://doi.org/10.1016/j.msea.2017.02.104>.
- [73] C. Liu, Selective laser melting of nickel superalloys for aerospace applications: defect analysis and material property optimisation, *University of Sheffield* (2021), uk.bl.ethos.846612<https://doi.org/10.1016/j.mseaa.2006.30067>.
- [74] A. Jena, A. Gontcharov, S. Atabay, et al., Structure and properties of LW 4280, a new high γ' Ni-based superalloy fabricated by laser powder bed fusion, *Next Materials.* 1 (4) (2023) 100056, <https://doi.org/10.1016/j.nxmate.2023.100056>.
- [75] X. Cui, S. Zhang, C. Zhang, et al., Additive manufacturing of 24CrNiMo low alloy steel by selective laser melting: influence of volumetric energy density on densification, microstructure and hardness, *Mater. Sci. Eng. A* 809 (2021) 140957, <https://doi.org/10.1016/j.msea.2021.140957>.
- [76] B. AlMangour, D. Grzesiak, J. Cheng, et al., Thermal behavior of the molten pool, microstructural evolution, and tribological performance during selective laser melting of TiC/316L stainless steel nanocomposites: experimental and simulation methods, *J. Mater. Process. Technol.* 257 (2018) 288–301, <https://doi.org/10.1016/j.jmatprotec.2018.01.028>.
- [77] B. Stegman, A. Shang, L. Hoppenrath, et al., Volumetric energy density impact on mechanical properties of additively manufactured 718 Ni alloy, *Mater. Sci. Eng., A* 854 (2022) 143699, <https://doi.org/10.1016/j.msea.2022.143699>.
- [78] M. Ghayoor, K. Lee, Y. He, et al., Selective laser melting of 304L stainless steel: role of volumetric energy density on the microstructure, texture and mechanical properties, *Addit. Manuf.* 32 (2020) 101011, <https://doi.org/10.1016/j.addma.2019.101011>.
- [79] R. Zhao, C. Chen, W. Wang, et al., On the role of volumetric energy density in the microstructure and mechanical properties of laser powder bed fusion Ti-6Al-4V alloy, *Addit. Manuf.* 51 (2022) 102605, <https://doi.org/10.1016/j.addma.2022.102605>.
- [80] A. Simchi, Direct laser sintering of metal powders: Mechanism, kinetics and microstructural features, *Mater. Sci. Eng., A* 428(1-2) (2006) 148–158, <https://doi.org/10.1016/j.msea.2006.04.117>.
- [81] T. Guraya, S. Singamneni, Z. Chen, Microstructure formed during selective laser melting of INT38LC in keyhole mode, *J. Alloys Compd.* 792 (2019) 151–160, <https://doi.org/10.1016/j.jallcom.2019.03.419>.
- [82] C. Qiu, H. Chen, Q. Liu, et al., On the solidification behaviour and cracking origin of a nickel-based superalloy during selective laser melting, *Mater. Charact.* 148 (2019) 330–344, <https://doi.org/10.1016/j.matchar.2018.12.032>.
- [83] M. Calandri, Inconel 718 superalloy produced through Selective Laser Melting for harsh environment applications, *Dipartimento Scienza Applicata e Tecnologia, Politecnico di Torino*, (2019), <https://hdl.handle.net/11583/2739924>.
- [84] X. Yu, P. Song, X. He, et al., Influence of the combined-effect of NaCl and Na₂SO₄ on the hot corrosion behaviour of aluminide coating on Ni-based alloys, *J. Alloys Compd.* 790 (2019) 228–239, <https://doi.org/10.1016/j.jallcom.2019.03.165>.
- [85] B. Zhang, H. Yan, Z. Xia, et al., Influence of scanning strategy and post-treatment on cracks and mechanical properties of selective-laser-melted K438 superalloy, *Coatings* 14 (4) (2024) 414, <https://doi.org/10.3390/coatings14040414>.
- [86] X. Zhang, H. Chen, L. Xu, et al., Cracking mechanism and susceptibility of laser melting deposited Inconel 738 superalloy, *Mater. Des.* 183 (2019) 108105, <https://doi.org/10.1016/j.matdes.2019.108105>.
- [87] D. Holländer, D. Kulawinski, A. Weidner, et al., Small-scale specimen testing for fatigue life assessment of service-exposed industrial gas turbine blades, *Int. J. Fatigues* 92 (2016) 262–271, <https://doi.org/10.1016/j.ijfatigue.2016.07.014>.
- [88] Q. Wei, Y. Xie, Q. Teng, et al., Crack Types, Mechanisms, and Suppression Methods during High-energy Beam Additive Manufacturing of Nickel-based Superalloys: A Review, *Chin. J. Mech. Eng.: Addit. Manuf. Front.* 1(4) (2022) 100055, <https://doi.org/10.1016/j.cjimeam.2022.100055>.
- [89] Y. Tang, C. Panviswas, J. Ghoussoub, et al., Alloys-by-design: application to new superalloys for Additive Manufacturing, *Acta Mater.* 202 (2021) 417–436, <https://doi.org/10.1016/j.actamat.2020.09.023>.

- [90] X. Wang, L. Liu, T. Huang, et al., Grain boundary precipitation behavior in Re-containing nickel-based directionally solidified superalloys with carbon and boron additions, Vacuum 179 (2020) 109483, <https://doi.org/10.1016/j.vacuum.2020.109483>.
- [91] X. Zhao, X. Lin, J. Chen, et al., The effect of hot isostatic pressing on crack healing, microstructure, mechanical properties of Rene88DT superalloy prepared by laser solid forming, Mater. Sci. Eng., A 504(1-2) (2009) 129-134, <https://doi.org/10.1016/j.msea.2008.12.024>.
- [92] E. Bassini, A. Sivo, P. Martelli, et al., Effects of the solution and first aging treatment applied to as-built and post-HIP CM247 produced via laser powder bed fusion (LPBF), J. Alloys Compd. 905 (2022) 164213, <https://doi.org/10.1016/j.jallcom.2022.164213>.
- [93] J. Chen, M. Jin, K. Wei, et al., Laser-based powder bed fusion of nickel-based superalloy designed specifically for turbine blades using high-power flat-top laser: Towards high-speed manufacturing and directional solidification, J. Alloys Compd. 1022 (2025) 179902, <https://doi.org/10.1016/j.jallcom.2025.179902>.
- [94] F. Ghaini, M. Sheikhi, M. Torkamany, et al., The relation between liquation and solidification cracks in pulsed laser welding of 2024 aluminium alloy, Mater. Sci. Eng., A 519(1-2) (2009) 167-171, <https://doi.org/10.1016/j.msea.2009.04.056>.
- [95] N. Hatami, R. Babaei, M. Dadashzadeh, et al., Modeling of hot tearing formation during solidification, J. Mater. Process. Technol. 205 (1-3) (2008) 506-513, <https://doi.org/10.1016/j.jmatprotec.2007.11.260>.
- [96] A. Norman, V. Drachner, P. Prangnell, Effect of welding parameters on the solidi@cation microstructure of autogenous TIG welds in an Al-Cu-Mg-Mn alloy, Mater. Sci. Eng., A 259(1) (1999) 53-64, [https://doi.org/10.1016/S0921-5093\(98\)00873-9](https://doi.org/10.1016/S0921-5093(98)00873-9).
- [97] L. Shi, G. Niu, Y. Tan, et al., Investigation of the mechanical anisotropy of the hot isostatic pressing Mar-M247 produced via laser powder bed fusion (LPBF): a perspective on grain characteristics, Mater. Res. Express. 12(5)(2025)056506, <https://doi.org/10.1088/2053-1591/add650>.
- [98] Y. Chen, H. Chen, J. Chen, et al., Numerical and experimental investigation on thermal behavior and microstructure during selective laser melting of high strength steel, J. Manuf. Process. 57 (2020) 533-542, <https://doi.org/10.1016/j.jmapro.2020.06.041>.
- [99] J. Hunt, Steady State Columnar and Equiaxed Growth of Dendrites and Eutectic, Mater. Sci. Eng., A 65.1 (1984) 75-83, [https://doi.org/10.1016/0025-5416\(84\)90201-5](https://doi.org/10.1016/0025-5416(84)90201-5).
- [100] H. Zhang, H. Zhu, X. Nie, et al., Effect of Zirconium addition on crack, microstructure and mechanical behavior of selective laser melted Al-Cu-Mg alloy, Scripta Mater. 134 (2017) 6-10, <https://doi.org/10.1016/j.scriptamat.2017.02.036>.
- [101] J. Hu, Y. Shi, X. Sauvage, et al., Grain boundary stability governs hardening and softening in extremely fine nanograined metals, Science 355 (6331) (2017) 1292-1296, <https://doi.org/10.1126/science.aal5166>.
- [102] O. Adegoke, J. Andersson, H. Brodin, et al., Influence of laser powder bed fusion process parameters on the microstructure and cracking susceptibility of nickel-based superalloy Alloy 247LC, Results Mater. 13 (2022) 100256, <https://doi.org/10.1016/j.rimna.2022.100256>.
- [103] J. Park, S. Jun, B. Lee, et al., Alloy design of Ni-based superalloy with high γ' volume fraction suitable for additive manufacturing and its deformation behavior, Addit. Manuf. 52 (2022) 102680, <https://doi.org/10.1016/j.addma.2022.102680>.
- [104] P. Hu, Z. Liu, M. Chen, et al., Reducing cracking sensitivity of CM247LC processed via laser powder bed fusion through composition modification, J. Mater. Res. Technol. 29 (2024) 3074-3088, <https://doi.org/10.1016/j.jmrt.2024.02.082>.
- [105] A. Shaikh, Development of a γ' Precipitation Hardening Ni-Based Superalloy for Additive Manufacturing, Chalmers University of Technology (2018) 255645, <https://hdl.handle.net/20.500.12380/255645>.
- [106] S. Kou, A criterion for cracking during solidification, Acta Mater. 88 (2015) 366-374, <https://doi.org/10.1016/j.actamat.2015.01.034>.
- [107] D. Grange, J. Bartout, B. Macquaire, et al., Processing a non-weldable nickel-base superalloy by Selective Laser Melting: role of the shape and size of the melt pools on solidification cracking, Materialia 12 (2020) 100686, <https://doi.org/10.1016/j.jmtla.2020.100686>.
- [108] J. Xu, X. Lin, P. Guo, et al., The initiation and propagation mechanism of the overlapping zone cracking during laser solid forming of IN-738LC superalloy, J. Alloys Compd. 749 (2018) 859-870, <https://doi.org/10.1016/j.jallcom.2018.03.366>.
- [109] J. Xu, X. Lin, Y. Zhao, et al., HAZ liquation cracking mechanism of IN-738LC superalloy prepared by laser solid forming, Metall. Mater. Trans. A 49 (2018) 5118-5136, <https://doi.org/10.1007/s11661-018-4826-6>.
- [110] Z. Zhou, L. Huang, Y. Shang, et al., Causes analysis on cracks in nickel-based single crystal superalloy fabricated by laser powder deposition additive manufacturing, Mater. Des. 160 (2018) 1238-1249, <https://doi.org/10.1016/j.matdes.2018.10.042>.
- [111] N. Wang, S. Mokadem, M. Rappaz, et al., Solidification cracking of superalloy single- and bi-crystals, Acta Mater. 52 (11) (2004) 3173-3182, <https://doi.org/10.1016/j.actamat.2004.03.047>.
- [112] A. Hariharan, L. Lu, J. Risse, et al., Misorientation-dependent solute enrichment at interfaces and its contribution to defect formation mechanisms during laser additive manufacturing of superalloys, Phys. Rev. Mater. 3(12)(2019)123602, <https://doi.org/10.1103/PhysRevMaterials.3.123602>.
- [113] J. Yin, L. Yang, X. Yang, et al., High-power laser-matter interaction during laser powder bed fusion, Addit. Manuf. 29 (2019) 100778, <https://doi.org/10.1016/j.addma.2019.100778>.
- [114] K. Kosiba, T. Gustmann, J. Kim, et al., Experimental cooling rates during high-power laser powder bed fusion at varying processing conditions, J. Alloys Compd. 967 (2023) 171773, <https://doi.org/10.1016/j.jallcom.2023.171773>.
- [115] G. Huang, K. Wei, J. Deng, et al., High-power laser powder bed fusion of 316L stainless steel: Defects, microstructure, and mechanical properties, J. Manuf. Process. 83 (2022) 235-245, <https://doi.org/10.1016/j.jmapro.2022.08.066>.
- [116] D. Simson, C. Paul, S. Subbu, et al., Experimental study and neural network model based prediction of layer thickness influence on LPBF IN625 single track geometry, Opt. Laser Technol. 173 (2024) 110543, <https://doi.org/10.1016/j.optlastec.2024.110543>.
- [117] A. Pilehrood, H. Omidvar, A. Shamsipur, et al., Effect of transient liquid phase bonding followed by homogenization on the microstructure and hot tensile behavior of Inconel 738 superalloy, J. Manuf. Process. 48 (2019) 110-118, <https://doi.org/10.1016/j.jmapro.2019.10.030>.
- [118] O. Ogunbiyi, T. Jamiru, R. Sadiku, et al., Effects of sintering temperature on the microstructure, mechanical, tribological and thermophysical properties of GNPs/ INT38 composite, J. Mater. Res. Technol. 23 (2023) 5587-5605, <https://doi.org/10.1016/j.jmrt.2023.02.166>.
- [119] B. Zhang, H. Yan, Z. Xia, et al., Influence of Scanning Strategy and Post-Treatment on Cracks and Mechanical Properties of Selective-Laser-Melted K438 Superalloy, Coatings 14(4)(2024) 414, <https://doi.org/10.3390/coatings14040414>.
- [120] T. Bhardwaj, M. Shukla, Effect of laser scanning strategies on texture, physical and mechanical properties of laser sintered maraging steel, Mater. Sci. Eng., A 734 (2018) 102-109, <https://doi.org/10.1016/j.msea.2018.07.089>.
- [121] B. Kumar, S. Sahu, D. Srinivasan, et al., Influence of heat input on solidification cracking in additively manufactured CM247LC Ni-based superalloy, Metall. Mater. Trans. A 54 (6) (2023) 2394-2409, <https://doi.org/10.1007/s11661-023-07027-7>.
- [122] L. Liu, D. Wang, G. Deng, et al., Crack inhibition and mechanical property enhancement of a CM247LC alloy fabricated by laser powder bed fusion through remelting strategy, Mater. Charact. 214 (2024) 114073, <https://doi.org/10.1016/j.jmatchar.2024.114073>.
- [123] S. Luo, W. Huang, H. Yang, et al., Selective laser melting of the hard-to-weld INT38LC superalloy: efforts to mitigate defects and the resultant microstructural and mechanical properties, J. Alloys Compd. 807 (2019) 151662, <https://doi.org/10.1016/j.jallcom.2019.151662>.
- [124] H. Wang, X. Zhang, G.B. Wang, et al., Microstructural evolution and corrosion behaviors of Inconel 718 alloy produced by selective laser melting following different heat treatments, Addit. Manuf. 30 (2019) 100875, <https://doi.org/10.1016/j.addma.2019.100875>.
- [125] O. Messé, R. Moreno, T. Illston, et al., Metastable carbides and their impact on recrystallization in INT38LC processed by selective laser melting, Addit. Manuf. 22 (2018) 394-404, <https://doi.org/10.1016/j.addma.2018.05.030>.
- [126] J. Boswell, D. Clark, W. Li, et al., Cracking during thermal post-processing of laser powder bed fabricated CM247LC Ni-superalloy, Mater. Des. 174 (2019) 107793, <https://doi.org/10.1016/j.matdes.2019.107793>.
- [127] D. Wang, Z. Liu, G. Deng, et al., A laser powder bed fusion-based methodology for repairing damaged nickel-based turbine blades: investigation of interfacial characteristics and hot isostatic pressing treatment, Mater. Charact. 212 (2022), <https://doi.org/10.1016/j.jmatchar.2024.113948>.
- [128] J. Bi, L. Wu, S. Li, et al., Beam shaping technology and its application in metal laser additive manufacturing: a review, J. Mater. Res. Technol. 26 (2023) 4606-4628, <https://doi.org/10.1016/j.jmrt.2023.08.037>.
- [129] C. Lun, Q. Wang, B. Gu, et al., Polycrystalline γ-TiAl alloys microstructural evolution and defect analysis during LPBF process by molecular dynamics simulation, J. Cryst. Growth 667 (2025) 128249, <https://doi.org/10.1016/j.jcrysgro.2025.128249>.
- [130] Y. Qiu, T. Yang, H. Zhu, et al., Dynamic behavior and defect control in LPBF of quartz glass: Insights from VOF model simulations, Powder Technol. 451 (2025) 120450, <https://doi.org/10.1016/j.powtec.2024.120450>.
- [131] Z. Xu, C. Jiang, R. Liu, et al., Corrosion and tribocorrosion resistance of superhydrophobic LPBF-NiTi alloys surface fabricated by nanosecond laser and ultrasonic fluorination, Surf. Coat. Technol. 490 (2024) 131176, <https://doi.org/10.1016/j.surfcoat.2024.131176>.